

# Towards resolving bedload flux variability

Thomas Pähtz<sup>1,2,\*</sup>, Yulan Chen<sup>1</sup>, Jiafeng Xie<sup>1,3</sup>, Rémi Monthiller<sup>4</sup>, Raphaël Maurin<sup>5</sup>, Katharina Tholen<sup>6</sup>, Yen-Cheng Lin<sup>7</sup>, Hao-Che Ho<sup>7</sup>, Peng Hu<sup>1,†</sup>, Zhiguo He<sup>1,‡</sup>, and Orencio Durán<sup>8</sup>

<sup>1</sup>*Institute of Port, Coastal and Offshore Engineering, Ocean College, Zhejiang University, 316021 Zhoushan, China*

<sup>2</sup>*Donghai Laboratory, 316021 Zhoushan, China*

<sup>3</sup>*State Key Laboratory of Fluid Power and Mechatronic Systems and Department of Engineering Mechanics, Zhejiang University, Hangzhou 310027, China*

<sup>4</sup>*Aix-Marseille University, CNRS, Centrale Marseille, Institut de Recherche sur les Phénomènes Hors Équilibre (IRPHE), Marseille 13384, France*

<sup>5</sup>*Institut de Mécanique des Fluides de Toulouse (IMFT), Université de Toulouse, CNRS, F-31400 Toulouse, France*

<sup>6</sup>*Institute for Theoretical Physics, Leipzig University, Postfach 100920, 04009 Leipzig, Germany*

<sup>7</sup>*Department of Civil Engineering, National Taiwan University, Taipei City 106, China and*

<sup>8</sup>*Department of Ocean Engineering, Texas A&M University, College Station, Texas 77843-3136, USA*

(Dated: April 12, 2024)

Bedload transport occurs when a bed composed of sedimentary grains becomes mobile in response to the shearing by a flow of liquid. It shapes the landscapes of Earth and other planetary bodies by promoting the formation and growth of various multiscale geological features. Estimating the rate at which such processes take place requires accurate bedload flux predictions. However, even for highly idealized conditions in the laboratory, study-to-study variability of reported bedload flux measurements borders an order of magnitude. This uncertainty stems from physically poorly supported, typically empirical methods of determining the transport-driving bed shear stress, especially for very narrow or shallow channel flows, and from study-to-study grain shape variations. Here, we derive a non-empirical method of bed shear stress determination and apply it to a number of independent grain-shape-controlled data sets, based on well-controlled experiments and CFD-DEM simulations, for a very diverse range of transport conditions. An existing physical bedload model, here generalized to account for grain shape variability, predicts almost all these data within a factor of 1.3, whereas a prominent alternative model (Deal et al., *Nature* **613**, 298-302, 2023) seems falsified.

Bedload transport is a special kind of sediment transport in which typically coarse sedimentary grains roll, slide, and hop along the surface in response to the shearing of a loose granular bed by a flow of liquid. It plays a vital role in shaping the environments of Earth and other planetary bodies [1] by promoting the formation and growth of geological features of various scales, including ripples and dunes [2, 3], deltas and fans [4], and laminations and cross-bedding [5, 6]. A key problem hampering our understanding of bedload-induced landscape evolution is the notoriously large noise commonly associated with measurements of bedload flux, often exceeding an order of magnitude [7, 8]. It partially originates from huge non-Gaussian flux fluctuations over large time scales, which even occur under steady flow conditions in the laboratory due to continuous topographic change [9]. However, also when restricted to steady flows over flat beds at short timescales, reported bedload fluxes can still substantially differ between laboratory studies for largely self-similar conditions [8], and it has been unclear whether such differences arise due to physical or experimental reasons. On the one hand, physical reasons may come into play because dissimilarities in grain size and shape distributions are not accounted for by commonly used similarity parameters. On the other hand, study-to-study variability of the geometry of laboratory

facilities is a potential culprit on the experimental side, especially in view of the associated large random and systematic uncertainties in the experimental determination of the driving shear stress [10]. Focusing here on rectangular open channels, since they are geometrically similar to natural streams, the distance between the channel sidewalls  $b$  relative to the water depth  $h$  above the bed surface is a crucial parameter in this regard. Ideally, one would want  $b/h$  to be as large as possible to most closely resemble bedload transport in nature. However, in experimental reality,  $b/h$  is often of order unity, substantially weakening the shearing of the bed due to frictional losses at the sidewalls, causing the flow to be nonuniform in the cross-channel direction [11].

In an attempt to understand the origin of bedload flux variability in nature, Zhang et al. [12, 13] conducted grain-resolved numerical simulations of steady state gravel transport by turbulent water flow in which they varied a number of control parameters, including grain shape, and studied their effects on bedload flux. Furthermore, almost the same authors, Deal et al. [14], carried out laboratory experiments to measure bedload flux for various grain shapes. Based on their numerical and experimental data, they concluded that grain shape is a key contributor to bedload flux variability and derived a semiempirical bedload flux model correcting for

grain shape effects. However, since these data were solely obtained from laboratory and numerical experiments in a very narrow channel ( $b/h \approx 10^{-1}$ ), merely two grain diameters wide, one may question whether their model can be reliably applied to the typically much wider streams in nature ( $b/h \sim 10^0 \dots 10^3$ ). They attempted to account for their low  $b/h$ -ratio through an empirical correction of the driving shear stress. However, their corrected data of the nondimensionalized bedload flux for spherical grains differ from older measurements for much wider and shallower channel flows [15] by a factor of 4 to 6 at the same nondimensionalized bed shear stress, much more than the grain-shape-associated variability in their experiments.

Here, we compile existing and new data of turbulent bedload transport of shape-controlled grains, obtained from well-controlled experiments and grain-resolved and grain-unresolved numerical simulations based on various CFD-DEM (Computation Fluid Dynamics - Discrete Element Method) techniques, across channel flow widths and heights, grain shapes, bed slopes, and flow strengths. In spite of the considered very diverse range of methods and transport conditions, all data paint a consistent picture after employing a non-empirical sidewall correction, which we derive from Kolmogórov's theory of turbulence [16, 17], and a granular-physics-based method to precisely determine the bed surface elevation [18]. In particular, predictions from an existing physical bedload flux model [19], here straightforwardly generalized to account for grain shape variability, agree with the entire data compilation within a factor of 1.3, whereas Deal et al.'s [14] model seems falsified as it clearly disagrees with some of the data.

## TURBULENT BEDLOAD TRANSPORT OF SPHERICAL GRAINS

In order to evaluate grain shape effects on bedload flux, one first must ensure that existing data sets for spherical grains are consistent with one another. However, surprisingly, even though turbulent bedload transport has been studied for more than a century [20], flux measurements for spherical grains with a nearly uniform size distribution seem to be exceedingly scarce. After an extensive literature search, we have managed to find only a handful of data sets [14, 15, 21–24]. Four of these were subsequently disregarded because of either partially crystallized beds and very large scatter [21, 22], or the presence of substantial suspended load in addition to bedload [23], or self-inconsistent data [24] (almost no dependence of bedload flux with important variation of flow strength: increasing slope at constant water depth). We supplemented the remaining data compilation with additional data sets from numerical simulations that couple the DEM for the particle phase with a CFD method for the fluid phase that resolves the sub-grain scale: two data sets based on Direct

Numerical Simulations (DNS) [25, 26] for infinitely wide channels ( $b/h = \infty$ , i.e., periodic boundaries) and two data sets based on particle-resolving Large Eddy Simulations (LES) [12], one for  $b/h = \infty$  and one for a very-narrow-channel configuration ( $b/h \approx 0.1$ ). Only such high-end methods, because they do not coarse-grain the particle phase and do not rely on empiricism for fluid-particle interactions, can be considered as similarly reliable as controlled experiments [27]. Table I summarizes the data shown in this study, including those for experiments and grain-resolved simulations with non-spherical grains [13, 14, 28] and those from grain-unresolved CFD-DEM simulations (Refs. [19, 29, 30] and new simulations) discussed later.

The driving-flow strength in the experiments and grain-resolved simulations is quantified by the bed shear stress  $\tau_b$ , which is the fluid shear stress above the bedload transport layer extrapolated to the bed surface elevation within the fluid-particle mixture (Methods). In wide channels, if the bedload layer extends too close to the free surface of the liquid,  $\tau_b$  is sensitive to the precise definition of this elevation via the latter's influence on  $h$ . For such situations, we employ a granular-physics-based definition [18] (Methods). Otherwise, we use the values of  $h$  reported in the respective studies. In addition,  $\tau_b$  accounts for the presence of sidewalls through a non-empirical method we derived from Kolmogórov's theory of turbulence [16, 17] (Methods). It is smaller than the sidewall-free bed shear stress  $\tau_{bo} \equiv (\langle \chi \rangle_z + \rho_f g \sin \alpha) h$  (Methods), where  $\rho_f$  is the fluid density,  $g$  the gravitational acceleration,  $\alpha$  the bed slope angle, and  $-\langle \chi \rangle_z$  the height-averaged streamwise pressure gradient ( $\chi = 0$  except for pressure-driven simulations).

The hydrodynamic conditions are characterized by the particle-fluid density ratio  $s \equiv \rho_p/\rho_f$ , Galileo number  $Ga \equiv d\sqrt{s\tilde{g}_z d}/\nu$  (with  $d$  the grain diameter,  $\nu$  the kinematic fluid viscosity, and  $\tilde{g}_z \equiv (1 - 1/s)g \cos \alpha$  the vertical submerged gravity), Shields number  $\Theta \equiv \tau_b/(\rho_p \tilde{g}_z d)$ , dimensionless water depth  $h^* \equiv h/d$ , and slope angle  $\alpha$  (Table I). All data sets are well within the range of what is typically categorized as bedload transport ( $s \lesssim 10$  [19]), and most of them also satisfy  $s^{1/2}Ga \gtrsim 70$ , here termed “rough” conditions. In rough turbulent bedload, particle inertia dominate viscous fluid-particle interactions, and the nondimensionalized bedload flux  $Q_* \equiv Q/(\rho_p d\sqrt{s\tilde{g}_z d})$  therefore becomes essentially independent of  $s$  and  $Ga$  [19, 20]. The data for rough turbulent bedload transport of spherical grains, indeed, collapse, within measurement uncertainty, on a universal  $Q_*(\Theta)$ -behavior (Fig. 1). The fact that this collapse includes data from a very large range of channel-width-to-depth ratios ( $b/h = 0.09 - \infty$ ) supports our bed surface definition and sidewall correction method. In contrast, the data set NC18EXP plotted with the originally reported values of  $\Theta$  [15], based on a different bed surface definition and uncorrected for sidewall friction, deviates

Experimental or numerical study	Width-to-depth ratio, $b/h$	Grain shape	Shape parameters			Hydrodynamic conditions			
			$S_f$	$C_D$	$\mu_s$	$s$	$Ga$	$\alpha$	$h^*$
D23EXPs [14]	0.09–0.16 (narrow)	spheres	1	0.43	0.46	2.57	1334–1339	0.03–0.13	13–24
D23EXPe [14]	0.10–0.14 (narrow)	ellipsoids	0.83	0.60	0.60	2.42	1312–1314	0.03–0.09	15–22
D23EXPc [14]	0.10–0.13 (narrow)	chips	0.51	0.39	0.65	2.36	767–768	0.04–0.08	22–29
D23EXPg [14]	0.10–0.15 (narrow)	gravel	0.68	0.54	0.78	2.48	733–735	0.04–0.11	20–32
D23EXpp [14]	0.09–0.12 (narrow)	prisms	0.88	0.79	0.86	2.40	725	0.03–0.06	26–35
NC18EXP [15]	5.2–7.5 (wide)	spheres	1	0.49	0.45	1.39	998	0.02–0.03	2.3–3.3
R22EXPc [28]	5.5–5.6 (wide)	cylinders	0.84	0.32	0.60	1.42	738	0.05–0.06	8.4–14
R22EXPl [28]	5.0–5.8 (wide)	lenses	0.55	0.45	0.62	1.37	196	0.03–0.05	15–17
Z22LESn [12]	0.15–0.16 (narrow)	spheres	1	0.48	0.45	2.55	1354–1357	0.04–0.10	13–14
Z23LES [13]	0.09–0.10 (narrow)	gravel	0.67	0.71	0.75	2.47	718–719	0.03–0.10	32–33
Z22LESw [12]	$\infty$ (wide)	spheres	1	0.48	0.45	2.55	1378	0.01–0.03	4.6–22
J21DNS [25]	$\infty$ (wide)	spheres	1	N/A	N/A	2.55	44.7	0 ( $\chi > 0$ )	$\approx 18$
KU17DNS [26]	$\infty$ (wide)	spheres	1	N/A	N/A	2.5	28.37	0 ( $\chi > 0$ )	$\approx 13$
M18RANS [29]	$\infty$ (wide)	spheres	1	0.42	0.40	1.75–4	1259–2521	0.01–0.19	2.0–62
M19RANSs [30]	$\infty$ (wide)	spheres	1	0.42	0.49	2.5	1782	0.05	4.1–18
M19RANSst1 [30]	$\infty$ (wide)	triplets	0.85	0.42	0.55	2.5	1782	0.05	6.1–26
M19RANSst2 [30]	$\infty$ (wide)	triplets	0.75	0.42	0.63	2.5	1782	0.05	8.0–33
M19RANSst3 [30]	$\infty$ (wide)	triplets	0.71	0.42	0.68	2.5	1782	0.05	9.9–40
M19RANSst4 [30]	$\infty$ (wide)	triplets	0.62	0.42	0.72	2.5	1782	0.05	12–47
M19RANSst5 [30]	$\infty$ (wide)	triplets	0.58	0.42	0.69	2.5	1782	0.05	14–55
LES	$\infty$ (wide)	spheres	1	0.54	0.49	2.56	1341	0 ( $\chi > 0$ )	18–22
LESCD	$\infty$ (wide)	spheres	1	1.78	0.49	2.56	1341	0 ( $\chi > 0$ )	20–23
BLRANS1	$\infty$ (wide)	spheres	1	2.24	0.38	[1.1, 2.65]	50	0–0.16	$\infty$
BLRANS2	$\infty$ (wide)	spheres	1	1.46	0.38	[1.1, 2.65]	100	0	$\infty$
BLRANS CD	$\infty$ (wide)	spheres	1	15.9	0.38	2.65	50	0	$\infty$

TABLE I. Summary of bedload flux data shown in this study. The top, middle, and bottom entries correspond to experiments, grain-resolved CFD-DEM simulations, and grain-unresolved CFD-DEM simulations, respectively. Those data of the data sets BLRANS1 and BLRANS2 with  $s = 2.65$  and  $\alpha = 0$  are from Ref. [19]. Note that the here listed values of  $C_D$ ,  $Ga$ , and  $h^*$  for the data of Refs. [12–14] (Z22LESx, Z23LES, D23EXPx) can differ from those reported in these references due to a different definition of  $d$ . In addition, we corrected a mistake made by Zhang et al. [13] (Methods).

by a factor of 4 to 6 from the collapse. Similarly, applying our bed surface definition but the classical sidewall correction method by Einstein and Johnson [31–33] yields nonsensical (even partially negative) values of  $\Theta$  for the very-narrow-channel data sets D23EXPs and Z22LESn (inset of Fig. 1).

### TEST OF DEAL ET AL.’S [14] ROUGH-BEDLOAD FLUX MODEL WITH INDEPENDENT DATA

For non-spherical grains, the grain diameter  $d$  requires a more general definition. Deal et al. [14] replaced  $d$  by the volume-equivalent sphere diameter  $d_0 \equiv \sqrt[3]{6V_p/\pi}$ , with  $V_p$  the grain volume, and used the modified Shield number  $\Theta^{\text{D23}} \equiv \tau_b/(\rho_p \tilde{g}_z d_0)$  and modified nondimensionalized bedload flux  $Q_*^{\text{D23}} \equiv Q/(\rho_p d_0 \sqrt{(s-1)gd_0})$  to quantify the flow strength and transport rate, respectively. They proposed that bedload flux data corresponding to different grain shapes collapse onto a single curve  $Q_*^{\text{D23}} = f[(C^*/\mu^*)\Theta^{\text{D23}}]$ , where  $C^*$  is a sphere-normalized effective fluid drag coefficient (Methods) and  $\mu^* \equiv (\mu_s - \tan \alpha)/(\mu_o - \tan \alpha)$  encodes the sphere-normalized shear resistance of an assembly of non-spherical grains, with  $\mu_s$  the tangent of the static angle

of repose and  $\mu_o = \tan 24^\circ$  its approximate value for spheres.

Deal et al. [14] validated their model with their bedload flux measurements for several grain shapes, conducted in a very narrow channel ( $b \approx 2d_0$ ), but not with other experimental data from independent sources. To test their model with independent data, we acquired the same spheres as those used in Ref. [15], from the same company, and measured  $\mu_s$  using the funnel method [34] in the manner described in Ref. [14]: by slowly pouring them onto an elevated disk bounded by a  $2d_0$ -high rim (Methods). The settling velocity  $v_s$ , required to determine  $C^*$  (Methods), is reported in Ref. [15]. Furthermore, we scoured the literature and found two more experimental data sets for non-spherical grains that can be used to test their model: the bedload flux measurements for cylinders and lenses of Ref. [28] (R22EXPx in Table I). For both grain shapes,  $v_s$  is given in Ref. [35], while  $\mu_s$  was measured using the funnel method in a box filled with water, which was sufficiently large to rule out potential box-sidewall friction effects (private correspondence with the authors). We confirmed with DEM simulations that different procedures of conducting the funnel method have only a small effect on  $\mu_s$  ( $< 5\%$ ) provided that a sufficiently large number of grains is used and that

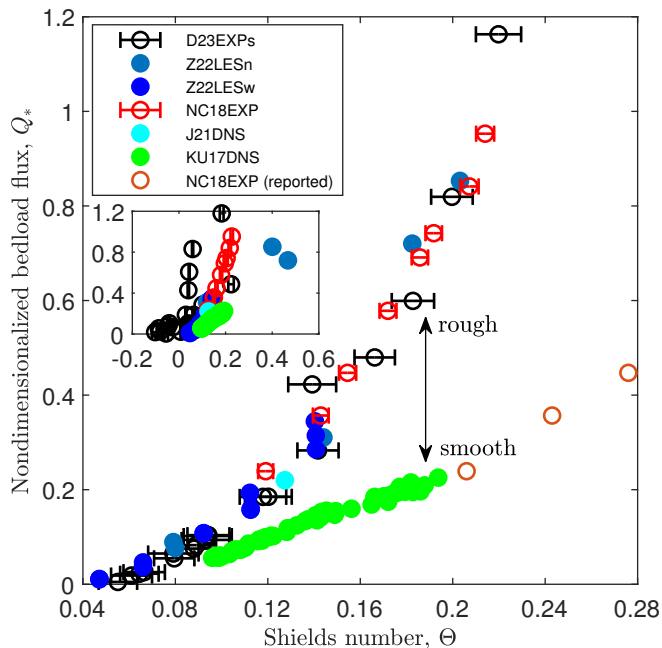


FIG. 1. Nondimensionalized bedload flux  $Q_*$  versus Shields number  $\Theta$  for spherical grains. Symbols correspond to data from experiments and grain-resolved simulations (Table I). An error bar indicates the standard error and/or uncertainty range of  $\Theta$  (Methods). In the absence of error bars, uncertainties are smaller than the symbol size. The arrow indicates the gap in the values of  $Q_*$  between the green ( $s^{1/2}Ga \simeq 44.86$ ) and other symbols ( $s^{1/2}Ga > 70$ ), corresponding to smooth and rough conditions, respectively. The data set NC18EXP plotted with the originally reported values of  $\Theta$  [15], based on a different bed surface definition and uncorrected for sidewall friction, deviates by about a factor of 4 to 6 from the other rough-conditions data, showcasing previous bedload flux variability due to poorly supported bed shear stress determination methods. Inset: The classical sidewall correction by Einstein and Johnson [31, 32], as described in Ref. [33], yields nonsensical (even partially negative) values of  $\Theta$  for the very-narrow-channel data sets D23EXPs and Z22LESn.

there is some means of preventing grains from rolling away (such as a rim or rough bed, see Methods).

The plots of the experimental and grain-resolved numerical data in terms of the dimensionless bedload flux  $Q_*^{D23}$  as a function of the shape-uncorrected ( $\Theta^{D23}$ ) and shape-corrected ( $\Theta^{D23}C^*/\mu^*$ ) Shields numbers are shown in Figs. 2(a) and 2(b), respectively. The empirical equation  $Q_*^{D23} = 12(\Theta^{D23} - 0.05)^{3/2}$  describes the uncorrected data quite well, which also happen to scatter much less than the corrected data for  $\Theta^{D23} \gtrsim 0.15$ . In particular, the data from Ref. [28], R22EXPC and R22EXPL, clearly disagree with the Deal et al.'s [14] Shields number correction and semiempirical model equation  $Q_*^{D23} = 12(\Theta^{D23}C^*/\mu^* - 0.05)^{3/2}$ .

So far, we have shown data from only well-controlled experiments and grain-resolved CFD-DEM simulations as they are the most realistic methods. Now, we add

data from grain-unresolved LES-DEM and RANS-DEM simulations to the compilation, both from existing studies [19, 29, 30] and from new simulations, all of which were conducted using either of the numerical models described in Refs. [36–38] (Methods, Table I). Although the latter are less realistic as they rely on semiempirical relations to calculate fluid-particle interaction forces (Methods), they can be used to confront bedload flux models with transport conditions across a much larger range of the control parameters  $\Theta$ ,  $\alpha$ , and  $h^*$ . They also allow us to perform gedankenexperiments in which  $C^*$  is treated as just another control parameter, since we can artificially modify  $C^*$  through changing the drag force parameters (Methods, LESCD and BLRANSCD in Table I). This is interesting because Deal et al.'s [14] model predicts a strong effect of  $C^*$  on  $Q_*$ . In fact, the data sets LESCD and BLRANSCD indicate that the  $C^*$ -modification of  $\Theta^{D23}$  proposed by these authors is fundamentally wrong as it massively shifts these data sets away from the other data (Figs. 2(c) and 2(d)).

### PHYSICAL ROUGH-BEDLOAD FLUX MODEL ACROSS GRAIN SHAPES, BED SLOPES, FLOW STRENGTHS, AND WATER DEPTHS

Using Reynolds-averaged numerical simulations (RANS) for the fluid phase coupled with the DEM for the motion of spherical grains, Pätz and Durán [19] simulated non-suspended sediment transport and derived a general transport rate expression holding for a large range of conditions, including turbulent bedload with  $s^{1/2}Ga \gtrsim 80$  and windblown sand:

$$Q_* = 2\kappa^{-1}\sqrt{\Theta_t}M_*(1 + c_M M_*). \quad (1)$$

Here  $\kappa = 0.41$  is the von Kármán constant,  $\Theta_t$  the transport threshold value of  $\Theta$ , and  $M_* \equiv M/(\rho_p d)$ , with  $M$  the transport load, measures the number  $N$  of transported grains above a bed area of size  $\sim d^2$ . The term  $c_M M_*$ , with  $c_M = 1.7$  a constant parameter determined from the simulations, encodes the rate of collisions between transported grains ( $\propto M_*^2$ ) relative to that of grain-bed collisions ( $\propto M_*^1$ ). Equation (1) expresses the balance between global energy production due to drag (left-hand side) and energy dissipation due to grain contacts (right-hand side). In order to apply it to non-spherical grains, it is important to generalize  $d$  in a manner that retains  $M_* \sim N$ . Since grains transported at elevations close to the bed surface, where most transport takes place, tend to align their largest projected area  $A_p^{\max}$  parallel to the bed due to torque [13, 39], implying  $M \sim N\rho_p V_p/A_p^{\max}$ , this requirement begets  $d \equiv \frac{3}{2}V_p/A_p^{\max}$ . Introducing the longest ( $a$ ), intermediate ( $b$ ), and shortest ( $c$ ) axes of a grain, one can estimate  $V_p = \pi abc/6$  and  $A_p^{\max} = \pi ab/4$ , leading to  $d = c$ . With this definition of  $d$ , the data of  $Q_*$  from the entire data

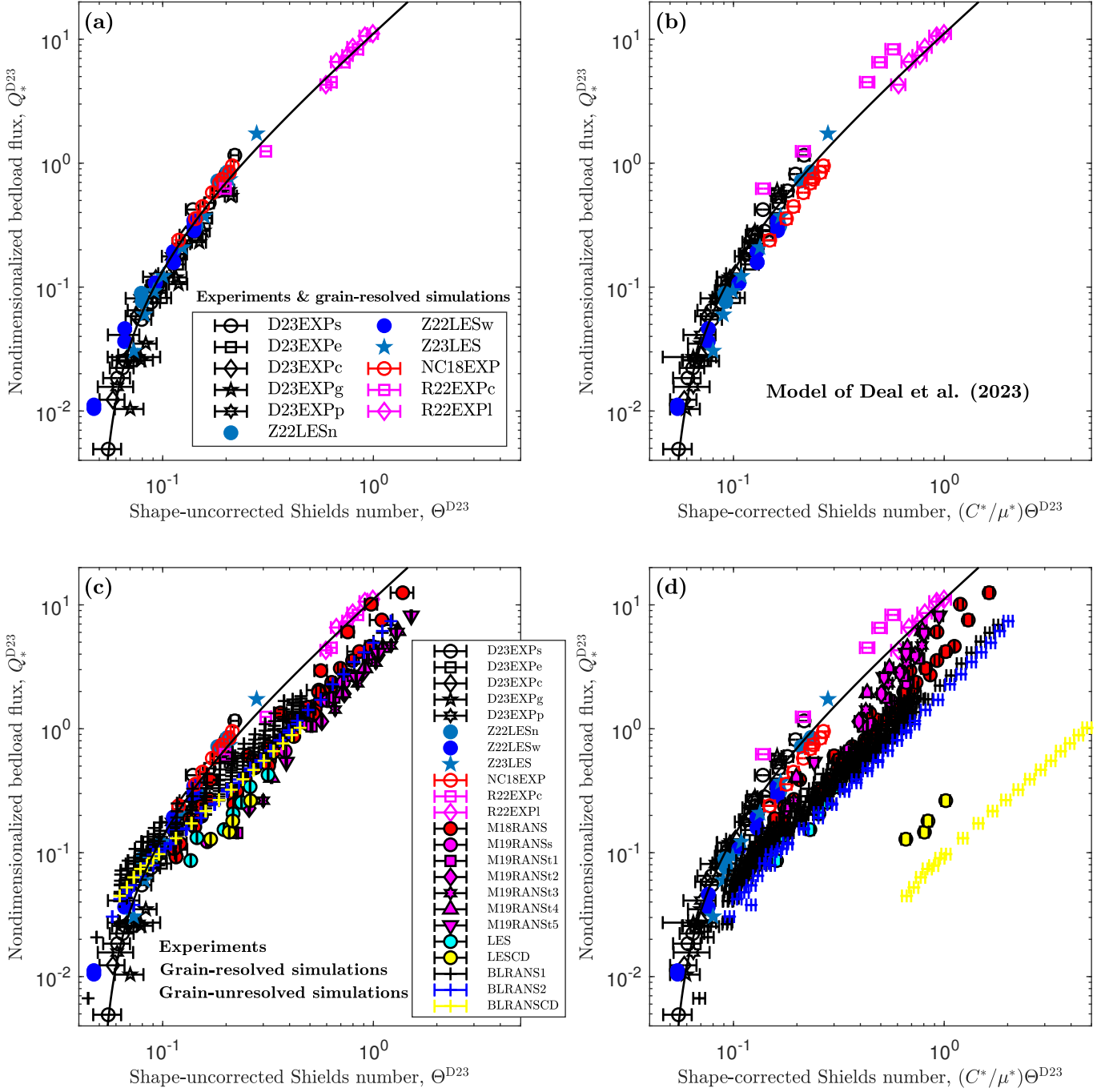


FIG. 2. Test of Deal et al.'s [14] bedload flux model unifying grain shape. Nondimensionalized bedload flux  $Q_*^{D23}$  versus shape-uncorrected Shields number  $\Theta^{D23}$  ((a) and (c)) and shape-corrected Shields number  $(C^*/\mu^*)\Theta^{D23}$  ((b) and (d)), based on the same definitions as in Ref. [14]. Symbols in (a) and (b) correspond to data from experiments and grain-resolved simulations (Table I). Symbols in (c) and (d) also include data from grain-unresolved simulations. An error bar indicates the propagated standard error and/or uncertainty range from  $C^*$ ,  $\mu^*$ , and  $\Theta$  (Methods). In the absence of error bars, uncertainties are smaller than the symbol size. The solid lines correspond to  $Q_*^{D23} = 12(\Theta^{D23} - 0.05)^{3/2}$  ((a) and (c)) and  $Q_*^{D23} = 12(\Theta^{D23} C^*/\mu^* - 0.05)^{3/2}$  ((b) and (d)), which is the model of Ref. [14].

compilation can vary by almost an order of magnitude at a given  $\Theta$  (Fig. 3).

From the fluid and particle phase momentum balances, neglecting particle-sidewall friction, one can straightfor-

wardly derive (Methods)

$$M_* = \mu_{\dagger}^{-1}(\Theta - \Theta_t), \quad \text{with} \quad (2)$$

$$\mu_{\dagger} \equiv r_b \mu_s \left[ \frac{1 + \left( \frac{s \tan \alpha}{s-1} + \bar{\chi}^* \right) \bar{f}_L / \bar{f}_D}{1 + r_b \mu_s \bar{f}_L / \bar{f}_D} \right] - \tan \alpha,$$

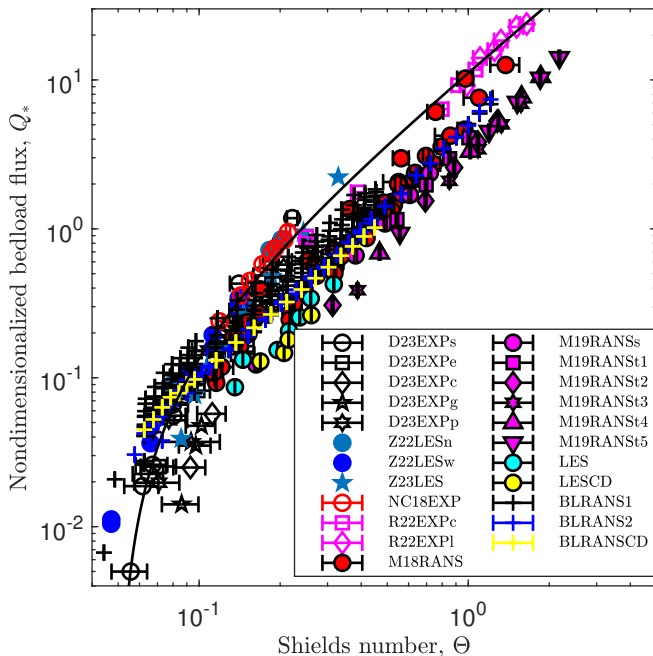


FIG. 3. Nondimensionalized bedload flux  $Q_*$  versus Shields number  $\Theta$ , both rescaled using the generalized grain diameter definition  $d \equiv \frac{3}{2}V_p/A_p^{\max}$  (see text). Symbols correspond to data from a variety of first-rate methods (Table I). An error bar indicates the propagated standard error and/or uncertainty range from  $\Theta$  (Methods). In the absence of error bars, uncertainties are smaller than the symbol size. The solid line corresponds to  $Q_* = 12(\Theta - 0.05)^{3/2}$ .

where  $\chi^* \equiv \chi/(\rho_p \tilde{g}_z)$ ,  $f_L$  and  $f_D$  are the lift and drag forces, respectively, per unit volume, and the overbar denotes the particle-concentration-weighted height average. Furthermore,  $r_b \equiv \mu_b/\mu_s > 1$  describes the increased shear resistance of the bed surface ( $\mu_b$ ) relative to that of the bulk ( $\mu_s$ ), since bedload transport strengthens the bed surface [40] (Methods).

The prefactor  $2\sqrt{\Theta_t}/\kappa$  in Eq. (1) resulted from interpreting  $\Theta_t$  as the smallest Shields number that permits a quasi-continuous hopping-rebound motion (saltation) of a test grain in a grain-motion-undisturbed logarithmic fluid velocity profile [19]. In such a scenario, lift forces acting on the moving test grain are typically much smaller than drag forces [41] due to the formers' rapid decrease with distance from the bed [42]. Then, despite the distinct underlying physical picture, it can be shown for conditions with  $s^{1/4}Ga \gtrsim 200$  that  $\Theta_t$  in Eq. (1) obeys a scaling classically associated with the drag-induced mobilization of a grain resting in a bed surface pocket [41]:

$$\Theta_t = c_t \left( r_b \mu_s - \frac{s \tan \alpha}{s - 1} \right) / C_D, \quad (3)$$

where  $c_t$  is a dimensionless parameter and  $C_D$  an effective drag coefficient parametrizing the streamwise drag force acting on grains, which depends on the settling velocity

$v_s$  and Corey shape factor  $S_f \equiv c/\sqrt{ab}$  (Methods). However, for  $s^{1/4}Ga \lesssim 200$ , viscous-sublayer effects render the scaling of  $\Theta_t$  much more complicated [41]. Therefore, we use Eq. (3) to determine  $\Theta_t$ , except for the few numerical conditions with  $s^{1/4}Ga < 200$  (BLRANSx in Table I), for which we determine  $\Theta_t$  directly from the simulations, as described in Ref. [19]. Note that the data sets J21DNS and KU17DNS in Table I, which also satisfy  $s^{1/4}Ga < 200$ , are excluded from this discussion as they violate the precondition  $s^{1/2}Ga \gtrsim 80$  for Eq. (1).

After fitting the model parameters to  $r_b = 1.8$ ,  $c_t = 0.032$ , and  $\overline{f_L}/\overline{f_D} = 1.2$  (except in the lift-force-neglecting grain-unresolved simulations, where  $f_L \equiv 0$ ), the bedload flux model deviates by less than a factor of 1.3 from almost all data (Fig. 4). These fit values are consistent with some direct estimations:  $r_b$  agrees with DEM-RANS simulations ( $\mu_s \approx 0.4$  and  $\mu_b \approx 0.7$  [18]), both  $r_b$  and  $c_t$  predict a  $\Theta_t$ -value for the data set NC18EXP that is almost equal to the local fluid shear stress at the bed surface (consistent with the theoretical expectation [18], see Methods), and  $\overline{f_L}/\overline{f_D} = 1.2$  is close to measurements of drag and lift forces acting on surface roughness elements, including grains in bed surface pockets [42, 43].

Given the large diversity of conditions and experimental and numerical methods (Table I), the level of agreement in Fig. 4 is remarkable. It suggests that, with the here employed methods of sidewall correction and bed surface determination, and the above physical model to predict the flux of rough bedload transport (applicable if  $s^{1/2}Ga \gtrsim 80$ , satisfied for most conditions in nature), bedload variability is largely diminished, at least for the idealized case considered here (steady flows over flat beds at short timescales). This is a prerequisite for discerning different sources of variability in the more complex situations typically encountered in nature.

## METHODS

### STREAMWISE MOMENTUM BALANCES AND BED SHEAR STRESS

#### Streamwise fluid momentum balance

For a statistically steady ( $\partial_t = 0$ ) and streamwise uniform ( $\partial_x = 0$ ) fluid-particle mixture flow in an open channel with sidewalls, the streamwise fluid momentum balance, averaged over time  $t$  and the flow direction  $x$ , reads [44]

$$\rho_f \partial_y \tilde{\epsilon} \tilde{u}_y \tilde{u}_x + \rho_f \partial_z \tilde{\epsilon} \tilde{u}_z \tilde{u}_x = \partial_y \tilde{\tau}_{yx}^f + \partial_z \tilde{\tau}_{xz}^f + \tilde{\chi} + \rho_f \tilde{\epsilon} g \sin \alpha - \rho_p \tilde{\phi} \tilde{f}_x^{f \rightarrow p}, \quad (4)$$

where  $\rho_p$  and  $\rho_f$ ,  $g$ ,  $\alpha$ ,  $\tilde{\epsilon}$  and  $\tilde{\phi} = 1 - \tilde{\epsilon}$ ,  $\tilde{\mathbf{u}}$ ,  $\tilde{\tau}_{ij}^f$ , and  $\tilde{\mathbf{f}}^{f \rightarrow p}$  are the particle and fluid density, gravitational

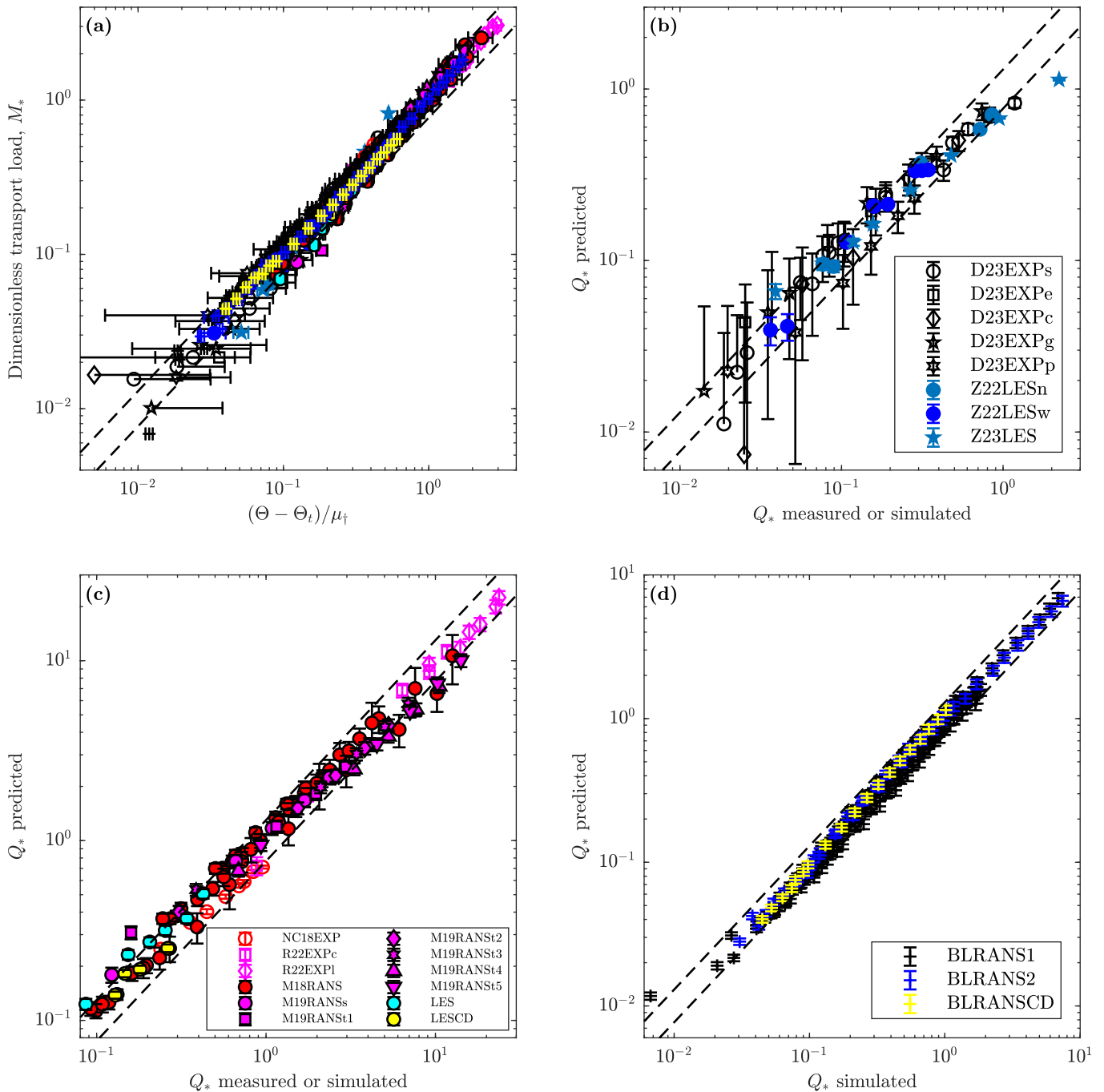


FIG. 4. Test of our bedload flux model across grain shapes, bed slopes, flow strengths, and water depths. (a) Nondimensionalized transport load  $M_*$ , calculated from the  $Q_*$ -data via Eq. (1), versus  $(\Theta - \Theta_t)/\mu_*$ . (b)-(d)  $Q_*$  predicted by Eqs. (1) and (2) versus measured or simulated  $Q_*$ . Symbols correspond to data from a variety of first-rate methods (Table I). An error bar indicates the propagated standard error and/or uncertainty range from  $\Theta$  and  $\mu_s$  (Methods). In the absence of error bars, uncertainties are smaller than the symbol size. When  $s^{1/4}Ga \geq 200$ ,  $\Theta_t$  is calculated by Eq. (3). Otherwise (only BLRANSx),  $\Theta_t$  is determined directly from the simulations, as described in Ref. [19]. Almost all data fall within a factor of 1.3 of the model prediction, delineated by the dashed lines.

acceleration, slope angle, average fluid and particle volume fractions, fluid velocity, fluid shear stress tensor, and fluid-particle interaction force per unit mass, respectively, and  $-\tilde{\chi}$  is a streamwise pressure gradient ( $\chi = 0$

except for the pressure-driven bedload transport simulations). Further averaging over the cross-channel direction  $y \in (-b/2, b/2)$ , with  $y = 0$  the channel center and  $b$  the

channel width, then yields

$$d_z(\tau_{xz}^f - \rho_f \epsilon u_z u_x) = 2(\tilde{\tau}_w^f - \rho_f \tilde{\epsilon}_w \tilde{u}_{w\perp} \tilde{u}_{w\parallel})/b - \chi - \rho_f \epsilon g \sin \alpha + \rho_p \phi f_x^{f \rightarrow p}, \quad (5)$$

where  $\tilde{\tau}_w^f \equiv \mp \tilde{\tau}_{yx}^f(\pm b/2)$ ,  $\tilde{\epsilon}_w \equiv \tilde{\epsilon}(\pm b/2)$ ,  $\tilde{u}_{w\perp} \equiv \mp \tilde{u}_y(\pm b/2)$  and  $\tilde{u}_{w\parallel} \equiv \tilde{u}_x(\pm b/2)$  are the fluid shear stress, average fluid volume fraction, average normal and tangential fluid velocities, respectively, at the sidewalls, and quantities without a tilde are analogous to those with a tilde but with respect to the overall average over  $t$ ,  $x$ , and  $y$ . In particular, the fluid shear stress  $\tau_{xz}^f$  of the overall average fluid momentum balance reads

$$\tau_{xz}^f = \langle \tilde{\tau}_{xz}^f \rangle_y - \rho_f \epsilon \langle \tilde{u}'_x \tilde{u}'_z \rangle_y^f, \quad (6)$$

where  $\tilde{\mathbf{u}}' \equiv \tilde{\mathbf{u}} - \mathbf{u}$  is the fluctuation fluid velocity with respect to the fluid-phase-weighted cross-channel average, defined as  $\langle \cdot \rangle_y^f \equiv \langle \tilde{\epsilon} \cdot \rangle_y / \epsilon$ , with  $\langle \cdot \rangle_y$  the cross-channel average. Finally, integration of Eq. (5) from the bed surface elevation  $z = 0$  to the water depth elevation  $z = h$ , exploiting that  $\tau_{xz}^f(h)$  and the boundary-averaged normal fluid fluxes  $\epsilon(0)u_z(0)$  and  $\langle \tilde{\epsilon}_w \tilde{u}_{w\perp} \rangle_z$  approximately vanish, with  $\langle \cdot \rangle_z \equiv \frac{1}{h} \int_0^h \cdot dz$  the height average, yields

$$\tau_{xz}^f(0) = (\langle \chi \rangle_z + \rho_f g \sin \alpha) h - 2h\tau_w^f/b - M \left( s^{-1} g \sin \alpha + \bar{f}_x^{f \rightarrow p} \right), \quad (7)$$

where  $M \equiv \rho_p \int_0^h \phi dz$  is the transport load,  $s \equiv \rho_p / \rho_f$  the particle-fluid density ratio,  $\bar{\cdot} \equiv \langle \phi \cdot \rangle_z / \langle \phi \rangle_z$  the  $\phi$ -weighted height average, and  $\tau_w^f$  the average sidewall fluid shear stress, given by

$$\tau_w^f \equiv \langle \tilde{\tau}_w^f \rangle_z - \rho_f \langle \tilde{\epsilon}_w \rangle_z \langle \tilde{u}'_{w\perp} \tilde{u}'_{w\parallel} \rangle_z^f, \quad (8)$$

with  $\tilde{u}'_{w\perp, \parallel} \equiv \tilde{u}_{w\perp, \parallel} - \langle \tilde{u}_{w\perp, \parallel} \rangle_z^f$  the fluctuation sidewall fluid velocity with respect to the fluid-phase-weighted sidewall average, defined as  $\langle \cdot \rangle_z^f \equiv \langle \tilde{\epsilon}_w \cdot \rangle_z / \langle \tilde{\epsilon}_w \rangle_z$ .

### Streamwise particle momentum balance

Analogous to Eq. (7), the height-integrated overall average streamwise particle momentum balance reads [44]

$$\sigma_{xz}^p(0) = -2h\tau_w^p/b + M \left( g \sin \alpha + \bar{f}_x^{f \rightarrow p} \right), \quad (9)$$

where  $\tau_w^p$  the average sidewall particle shear stress and  $\sigma_{ij}^p$  the particle stress tensor. They consist of contributions from the particle fluctuation motion, local contact forces, and the grains' rotational motion (for precise definitions, see Ref. [44]).

### Streamwise mixture momentum balance and bed shear stress definition

Summing Eqs. (5) and (9) yields the streamwise mixture balance:

$$\tau_{xz}^f(0) + \sigma_{xz}^p(0) = \tau_b + M\tilde{g}_z \tan \alpha, \quad (10)$$

where  $\tilde{g}_z \equiv (1 - 1/s)g \cos \alpha$  is the vertical submerged gravity and  $\tau_b$  the bed shear stress, defined as

$$\tau_b \equiv (\langle \chi \rangle_z + \rho_f g \sin \alpha) h - \frac{2h}{b}\tau_w \equiv \tau_{bo} - \frac{2h}{b}\tau_w, \quad (11)$$

with  $\tau_w \equiv \tau_w^f + \tau_w^p$  the mixture sidewall shear stress.

### Streamwise fluid momentum balance for flow in an inner turbulent boundary layer

The model of Ref. [36] considers a flow in an inner turbulent boundary layer of infinite height (no sidewalls). To be consistent with Eq. (10), we slightly modified the streamwise momentum balance in Ref. [36] to

$$d_z \tau_{xz}^f = \rho_f \phi g \sin \alpha + \rho_p \phi f_x^{f \rightarrow p}, \quad \text{with} \quad \tau_{xz}^f(\infty) = \tau_b \quad (12)$$

before conducting simulations.

### Relationship between bed shear stress and logarithmic fluid velocity profile

For turbulent bedload transport in open channels, there is a limited region in the clear-water flow above the bedload layer where the fluid velocity profile approximately satisfies the logarithmic law of the wall [14, 25, 45]:

$$u_x \simeq \frac{u_\tau^{\log}}{\kappa} \ln \frac{z}{z_o}, \quad (13)$$

with  $\kappa = 0.41$  the von Kármán constant,  $z_o$  the hydrodynamic roughness, and  $u_\tau^{\log} \equiv \sqrt{\tau_{\log}} / \rho_f$  the friction velocity. In DNS simulations of bedload transport, the associated shear stress  $\tau_{\log}$  is equivalent to the bed shear stress defined by Eq. (11) [25, 45]:

$$\tau_{\log} \simeq \tau_b. \quad (14)$$

Although these simulations were conducted under zero-slope conditions in the absence of sidewalls, we assume that Eq. (14) holds true also under more general circumstances.

### NON-EMPIRICAL SIDEWALL CORRECTION

Equation (14) indicates that  $\tau_b$  can be understood as the value of  $\tau_{xz}^f(z)$  extrapolated from the particle-free region above the transport layer to the bed surface



$z = 0$ . In the same spirit, we interpret  $\tau_w$  as the value of  $\frac{1}{h-z} \int_z^h \left[ \tilde{\tau}_w^f(z') - \rho_f \tilde{\epsilon}_w \tilde{u}'_{w\perp} \tilde{u}'_{w\parallel} \right] dz'$  (cf. Eq. (8)), where the prime refers to fluctuations with respect to the fluid phase average over heights between  $z$  and  $h$ , extrapolated from the particle-free region to  $z = 0$ . Based on these interpretations, we assume that the ratio  $\tau_w/\tau_b$  can be modeled as if the flow above the bed was devoid of grains. Using Kolmogórov's theory of turbulence, it can be written as [16, 17]

$$\tau_w/\tau_b = u_w/u_b, \quad (15)$$

where  $u_b$  and  $u_w$  are the characteristic values of the largest normal velocities that turbulent eddies can generate near the sidewalls and bed surface, respectively. These are eddies of sizes controlled by the roughness size  $r$  of the rough bed and by the thickness  $5(\kappa_\epsilon \kappa_u^3/2)^{-1/4} R \Re^{-3/4}$  of the viscous sublayer adjacent to the smooth sidewalls, respectively. Here  $R \equiv hb/(b+2h)$  is the hydraulic radius,  $\Re \equiv UR/\nu$  the Reynolds number, with  $U$  the bulk fluid velocity and  $\nu$  the kinematic fluid viscosity,  $\kappa_\epsilon = 5/4$  a constant that follows from Kolmogórov's four-fifths law, and  $\kappa_u \equiv u_R/U$  a parameter that relates the characteristic velocity  $u_R$  of the largest eddies to  $U$ . It is found to be highly insensitive to flow geometry, with  $\kappa_u = 0.036 \pm 0.005$  measured in pipe flow [46] and  $\kappa_u = 0.033$  in the atmospheric boundary layer [47]. With these parameters,  $u_{w\perp}/u_{b\perp}$  can be calculated as [17]

$$\begin{aligned} \frac{u_w}{u_b} &= \frac{\left[ 5(\kappa_\epsilon \kappa_u^3/2)^{-1/4} R \Re^{-3/4} \right]^{1/3} \sqrt{(\beta/5)^{2/3} \Gamma_{-2/3}(\beta/5)}}{r^{1/3}} \\ &= c_{wb} \Re^{-1/4} (r/R)^{-1/3}, \quad \text{with } c_{wb} \simeq 2.23, \end{aligned} \quad (16)$$

where  $\beta = [3\Gamma(4/3)]^{3/4}$  is the characteristic constant of the exponential decay of the velocity spectrum of turbulent flow. Since grains transported at elevations close to the bed surface tend to align their largest projected area parallel to the bed due to torque [13, 39], we choose the shortest grain axis  $c$  as the parameter setting  $r$ , assuming that about half the grain size is protruding into the flow for water-worked beds:

$$r = c/2. \quad (17)$$

Combining Eqs. (11), (15), and (16) yields

$$\tau_b = \frac{\tau_{bo}}{1 + \frac{2h}{b} u_w/u_b}, \quad (18a)$$

$$\tau_b = \frac{\tau_{bo}}{1 + \frac{2h}{b} c_{wb} \Re^{-1/4} (r/R)^{-1/3}}. \quad (18b)$$

In order to apply Eq. (18b), one needs to know  $U$ , which we calculate from the measured fluid discharge  $Q_f$  as [28]

$$U = \frac{Q_f}{b \left( h - \int_0^h \phi dz \right)}. \quad (19)$$

Note that, except for intense sediment transport, the term  $\int_0^h \phi dz$  has only a marginal effect on  $\tau_b$ . Hence, for the data sets D23EXPx [14] (Table I), for which concentration profile data is not available, we calculate  $U$  as  $U \simeq Q_f/(bh)$ .

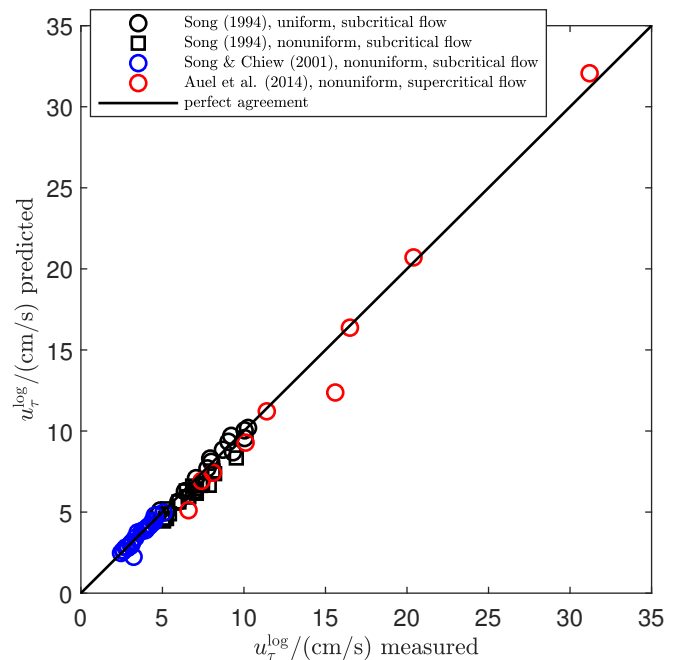


FIG. 5. Test of our non-empirical sidewall correction with experimental data from particle-free flows in open channels consisting of rough beds and smooth sidewalls [48–50] (data as summarized in the tables of Ref. [11]). Log-profile shear velocity  $u_\tau^{\log} = \sqrt{\tau_{\text{og}}/\rho_f}$  predicted by Eqs. (14) and (18b) versus measured one. For the nonuniform flows, the bed slope  $\tan \alpha$  is corrected using Eq. (1b) of Ref. [11]. The roughness sizes are  $r = c/2$  for the experiments of Ref. [48] (water-worked bed),  $r = d_0$  for those of Ref. [49] (sand grains glued on aluminum plate), and  $r = k$  for those of Ref. [50] (with  $k$  the measured absolute roughness).

The sidewall correction developed here is similar to the empirical one by Einstein and Johnson [31, 32], which can be summarized as [33]

$$\begin{aligned} \tau_b &= \rho_f g R_b \sin \alpha, \quad \text{with } R_b = (1 - 2R_w/b) \\ R_w &= f^{-1} R [6 \log_{10} [W(x)/x]]^{-2}, \\ f &= 8U^{-2} g R \sin \alpha, \quad x = [9\Re/(100f)]^{1/3}, \end{aligned} \quad (20)$$

where  $W(x)$  denotes the principal branch of the Lambert  $W$  function. In fact, the formal replacement  $u_w/u_b \rightarrow R_w/R_b$  in Eq. (18a), using  $R_b = (1 - 2R_w/b)$ , yields  $\tau_b = \rho_f g R_b \sin \alpha$ . Both methods seek to correct for the effect of sidewall friction relative to bed friction and both predict  $\tau_b \simeq \tau_R \equiv \rho_f g R \sin \alpha$  for flow in particle-free open channels with smooth sidewalls and beds, where this effect is negligible ( $u_w \simeq u_b$  and  $R_w \simeq R_b$ ). This prediction, though it has been critiqued for not accounting

for secondary currents [11], is consistent with measurements of  $\tau_{\text{log}}$  for a large range of width-to-depth ratios ( $b/h = 1.04\text{--}9.5$ ) [51]. Like Eq. (20) [11], Eq. (18b) is also consistent with measurements of  $\tau_{\text{log}}$  for particle-free flows in open channels consisting of rough beds and smooth sidewalls [48–50] (Fig. 5). The critical test for our and Einstein and Johnson’s method are the very-narrow channel bedload flux data sets D23EXPx [14] ( $b/h \approx 0.1$ , Table I). Applied to them, Eq. (20) yields nonsensical (even partially negative) values of  $\tau_b$  (inset of Fig. 1), whereas Eq. (18b) predicts  $\tau_b = (2.31\text{--}2.77)\tau_R$ , consistent with the rough empirical estimate  $\tau_{\text{log}} \approx 2.41\tau_R$  [14].

### Sidewall correction for LES simulations

The LES simulations with sidewalls of Refs. [12, 13] are only able to resolve flow structures that are about 15 times larger than the Kolmogórov length scale. One therefore expects that the above sidewall correction method, derived from Kolmogórov’s theory of turbulence, does not fully quantitatively capture their simulated conditions. To account for this, we multiply  $u_w/u_b$  in Eq. (18a) with a dimensionless correction coefficient  $c_{\text{LES}}$  of order unity, leading to

$$\tau_b = \frac{\tau_{bo}}{1 + \frac{2h}{b} c_{\text{LES}} c_{wb} \mathfrak{R}^{-1/4} (r/R)^{-1/3}}. \quad (21)$$

It is tuned to the value  $c_{\text{LES}} = 0.8$ , which ensures that the bedload flux data from the LES simulations for spherical grains of Ref. [12] (Z22LESn) collapse alongside the other spherical-grain data in Fig. 1.

### MAXIMUM FLUID SHEAR STRESS

An alternative measure for the driving shear stress is the maximum fluid shear stress [37]:

$$\tau_{\text{cl}} \equiv \max \tau_{xz}^f(z). \quad (22)$$

We use this definition in our grain-unresolved CFD-DEM simulations, since the raw data required to determine the bed surface elevation  $z = 0$ , and thus  $h$  and  $\tau_b$ , could no longer be located for the data sets M18RANS [29] and M19RANSx [30] (Table I). In contrast to  $\tau_b$ ,  $\tau_{\text{cl}}$  is not associated with the particle-fluid mixture but can be interpreted as an effective clear-water fluid shear stress acting on the top of the bedload layer [29]. Using  $\tau_b \propto h$  (Eq. (11)), it therefore defines an effective clear-water depth as

$$h_{\text{cl}} \equiv h \tau_{\text{cl}} / \tau_b \quad (23)$$

and subsequently an effective bedload thickness above the bed surface as

$$h_p \equiv h - h_{\text{cl}}. \quad (24)$$

The latter is linked to the transport load  $M$  via

$$M = \rho_p h_p \phi, \quad (25)$$

with  $\bar{\cdot} \equiv \frac{1}{h_p} \int_0^h \phi dz \approx \frac{1}{h_p} \int_0^{h_p} \cdot dz$  the approximate average of a particle quantity over the bedload thickness. Combining the above relations yields an expression linking the Shields numbers  $\Theta \equiv \tau_b / (\rho_p \tilde{g}_z d)$  and  $\Theta_* \equiv \tau_{\text{cl}} / (\rho_p \tilde{g}_z d)$  with one another:

$$\Theta = \Theta_* + \frac{\Theta_*}{\phi h_{\text{cl}}^*} M_*, \quad (26)$$

where  $h_{\text{cl}}^* \equiv h_{\text{cl}}/d$  and  $M_* \equiv M / (\rho_p d)$  are the dimensionless clear-water depth and transport load, respectively, with  $d$  the equivalent grain diameter. Note that, for our inner turbulent boundary layer simulations,  $h_{\text{cl}}^* = \infty$  and therefore  $\Theta = \Theta_*$ .

### TRANSPORT LOAD EXPRESSIONS

To derive simple expressions for the dimensionless transport load  $M_*$ , we henceforth neglect the contributions of particle-sidewall friction in the streamwise ( $\tau_w^p$  in Eq. (9)) and vertical particle momentum balances. Analogous to the former, the latter balance reads

$$d_z \sigma_{zz}^p = \rho_p \phi g \cos \alpha - \rho_p \phi f_z^{f \rightarrow p}. \quad (27)$$

In both balance equations, we separate fluid-particle interactions into buoyancy and non-buoyancy contributions. The latter are identified as the drag ( $f_D$ ) and lift ( $f_L$ ) forces per unit mass for the streamwise and vertical directions, respectively:

$$f_D \equiv f_x^{f \rightarrow p} - \chi / \rho_p, \quad (28a)$$

$$f_L \equiv f_z^{f \rightarrow p} - s^{-1} g \cos \alpha, \quad (28b)$$

where Eq. (28a) takes into account that buoyancy forces arise from instantaneous stresses, but not Reynolds stresses, and that the contribution of the instantaneous viscous shear stress to the streamwise buoyancy force can be neglected in turbulent bedload transport [29]. Using Eqs. (28a) and (28b), Eq. (9) and the integrated Eq. (27), respectively, become

$$\sigma_{xz}^p(0) = M (g \sin \alpha + \bar{\chi} / \rho_p + \overline{f_D}), \quad (29a)$$

$$\sigma_{zz}^p(0) = -M (\tilde{g}_z - \overline{f_L}). \quad (29b)$$

It follows that the bed friction coefficient, defined as  $\mu_b \equiv -\sigma_{xz}^p(0) / \sigma_{zz}^p(0)$ , constrains the average forces acting on transported grains:

$$\mu_b = \frac{g \sin \alpha + \bar{\chi} / \rho_p + \overline{f_D}}{\tilde{g}_z - \overline{f_L}}. \quad (30)$$

This equation can be transformed into

$$\overline{f_D} = \frac{\mu_b \tilde{g}_z - g \sin \alpha - \overline{\chi} / \rho_p}{1 + \mu_b \overline{f_L} / \overline{f_D}}. \quad (31)$$

Furthermore, combining Eq. (29a) with Eq. (10) and nondimensionalization leads to

$$\Theta - \Theta_{xz}^f(0) = M_* \left[ \left( \frac{s \tan \alpha}{s-1} + \overline{\chi}^* + \frac{\overline{f_D}}{\tilde{g}_z} \right) - \tan \alpha \right], \quad (32)$$

with  $\chi^* \equiv \chi / (\rho_p \tilde{g}_z)$  and  $\Theta_{xz}^f \equiv \tau_{xz}^f / (\rho_p \tilde{g}_z d)$ . Finally, insertion of Eq. (31), optionally using Eq. (26), yields

$$M_* = \mu_{\dagger}^{-1} [\Theta - \Theta_{xz}^f(0)], \quad (33a)$$

$$M_* = \left( \mu_{\dagger} - \frac{\Theta_*}{\phi h_{cl}^*} \right)^{-1} [\Theta_* - \Theta_{xz}^f(0)], \quad (33b)$$

$$\text{with } \mu_{\dagger} \equiv \mu_b \left[ \frac{1 + \left( \frac{s \tan \alpha}{s-1} + \overline{\chi}^* \right) \overline{f_L} / \overline{f_D}}{1 + \mu_b \overline{f_L} / \overline{f_D}} \right] - \tan \alpha.$$

### Exploiting bed surface properties

Up to this point, the only approximation involved in the derivation of Eqs. (33a) and (33b) is the disregard of particle-sidewall friction. Now, we apply two additional simplifications to obtain Eq. (2):

$$\mu_b = r_b \mu_s, \quad (34a)$$

$$\Theta - \Theta_{xz}^f(0) \approx \Theta - \Theta_t. \quad (34b)$$

Equation (34a) states that the bed friction coefficient  $\mu_b$  is proportional to the static friction coefficient  $\mu_s$ , defined as the tangent of the static angle of repose. The proportionality constant  $r_b > 1$  thereby takes into account that bedload transport increases the bed surface's ability to resist shear forces, since temporarily mobilized grains can settle again in more stable bed surface pockets [40]. The degree of bed surface strengthening depends on the characteristic velocity of transported grains, since fast grains tend to bypass the most stable pockets [40]. For viscous bedload transport, where the kinetic energy of transported grains is much smaller than potential wells of the bed surface, the bed surface resistance is strongest, with experiments [52] suggesting  $r_b \approx 3.4$  [41]. Equation (34b) could be interpreted as a consequence of  $\Theta_{xz}^f(0) \approx \Theta_t$ , which is Bagnold's hypothesis [53] that the near-surface flow velocity in bedload transport reduces to the threshold value that is barely sufficient to sustain grain motion. However, in actuality  $\Theta_{xz}^f(0) \approx \Theta_t$  is not a necessary requirement for Eq. (34b) to hold (for details see Ref. [18]). For Eqs. (34a) and (34b) to be justified, the bed surface elevation  $z = 0$  must be defined appropriately.

### Definition of bed surface elevation

Pächtz and Durán [18] defined the bed surface as the elevation at which the local production rate  $\sigma_{zz}^p \dot{\gamma}$ , with  $\dot{\gamma} \equiv d_z v_x$  the particle shear rate, of the cross-correlation particle fluctuation energy  $-\rho_p \phi v_x v_z$  is maximal. Their physical reasoning was based on an analogy to grain collisions with a rough base in inclined granular flows. They showed that, for data from DEM-RANS simulations of non-suspended sediment transport across a large range of bedload and windblown sand conditions, bed surfaces defined in this manner satisfy  $\mu_b \approx \text{const}$  and, for  $\Theta \lesssim 0.4$ ,  $\Theta_{xz}^f(0) \approx \Theta_t$ , consistent with the assumptions Eqs. (34a) and (34b). Since their simulations did not consider lift forces ( $f_L \equiv 0$ ), it follows from Eqs. (27) and (28b) that their definition was essentially equivalent to

$$\max(\dot{\gamma} \Sigma \phi) = [\dot{\gamma} \Sigma \phi]_{z=0}, \quad (35)$$

with  $\Sigma \phi(z) \equiv \int_z^h \phi(z') dz'$ .

### ESTIMATION OF BED SHEAR STRESS AND ITS UNCERTAINTY

We apply Eq. (35) to determine the bed surface elevation  $z = 0$ , and from it the flow depth  $h$ , for the experimental wide-channel data sets NC18EXP [15] and R22EXPx [28] (Table I), assuming that the reported time-averaged, local particle concentration and velocity profiles are proxies for the respective overall averages over  $t$ ,  $x$ , and  $y$ . Regarding velocity profiles, this standard assumption [11] is supported by measurements [50].

#### NC18EXP

For this highly-resolved data set, the profiles of  $\dot{\gamma} \Sigma \phi$  exhibit several local maximums due to layering (Fig. 6(a)). We choose the top-most local maximum at the bed surface elevation  $z = 0$  because the profiles  $\Theta_{xz}^f(z)$  exhibit a focal point there, with  $\Theta_{xz}^f(0) \approx \Theta_t$  (Fig. 7), consistent with the theoretical expectation [18]. It occurs  $\Delta z = 31.75 \pm 0.5$  mm above the channel bottom for all flow conditions. The upper and lower bounds  $\Delta z = 32.25$  mm and  $\Delta z = 31.25$  mm then yield corresponding lower ( $h_{\min}$ ) and upper ( $h_{\max}$ ) bounds, respectively, of  $h$  for a given flow condition, with corresponding bed shear stress estimates  $\tilde{\tau}_b(h_{\max})$  and  $\tilde{\tau}_b(h_{\min})$ , respectively, obtained from Eq. (18b). Hence, we estimate  $\tau_b$  and its uncertainty as

$$\tau_b = \frac{1}{2} [\tilde{\tau}_b(h_{\max}) + \tilde{\tau}_b(h_{\min})] \pm \frac{1}{2} [\tilde{\tau}_b(h_{\max}) - \tilde{\tau}_b(h_{\min})]. \quad (36)$$

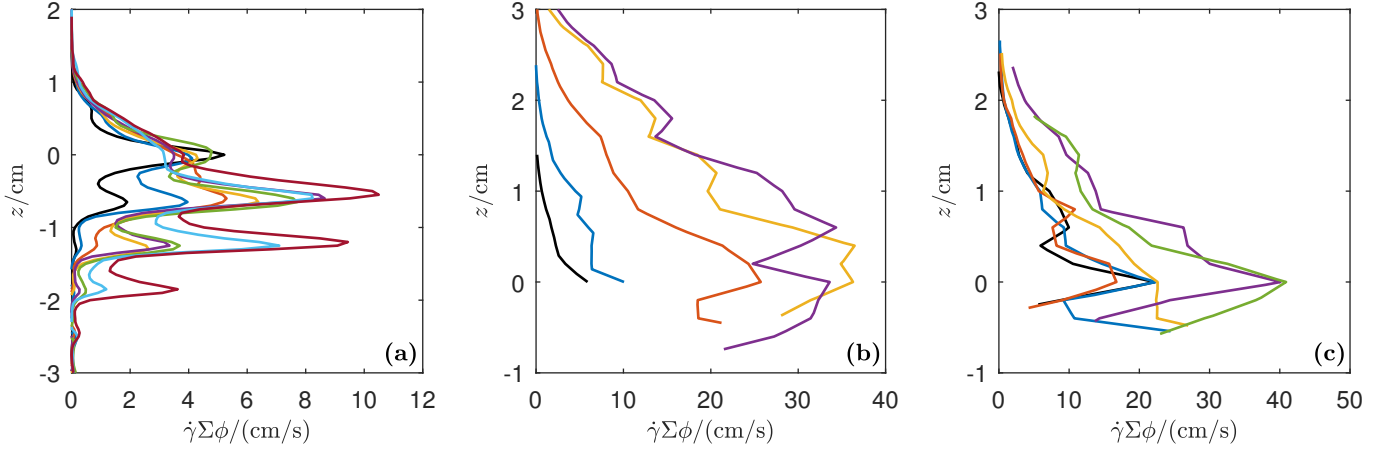


FIG. 6. Vertical profiles of  $\dot{\gamma}\Sigma\phi$  for the data sets (a) NC18EXP [15], (b) R22EXPc [28], and (c) R22EXPl [28] (Table I). They are used to determine the bed surface elevation  $z = 0$  in the manner described in the text.

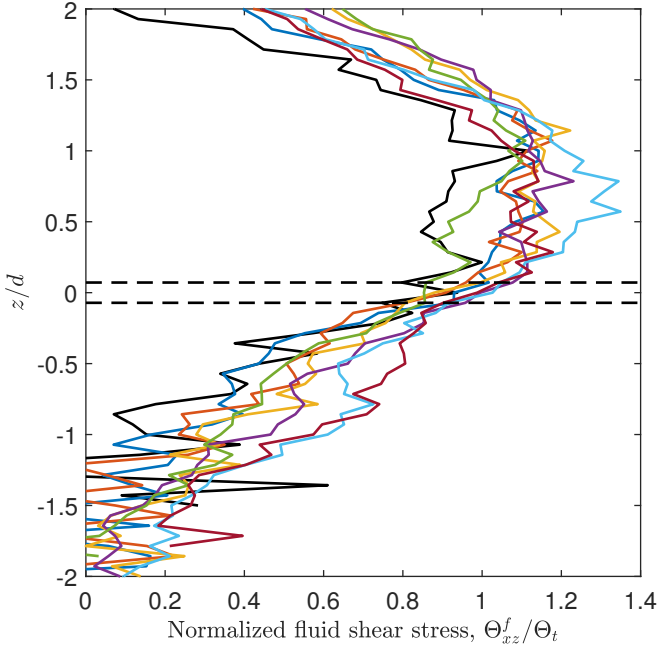


FIG. 7. Vertical profiles of the nondimensionalized fluid shear stress  $\Theta_{xz}^f$ , normalized by the threshold Shields number  $\Theta_t$  predicted by Eq. (3), for the data set NC18EXP [15]. The data exhibit a focal point at the bed surface elevation  $z = 0$ , where  $\Theta_{xz}^f \approx \Theta_t$ . The fluid shear stress  $\tau_{xz}^f$  is calculated from local quantities at the flume center as described in Ref. [54], assuming that the mixture viscosity obeys the closure measured by Boyer et al. [55] for viscous suspensions.

### R22EXPx

Two data sets are reported: one for cylindrical grains (R22EXPc) and one for grains with a lens shape (R22EXPl). Since the authors' experimental methods did not resolve  $v_x(z)$  inside the sediment bed [28] and

due to an insufficient data resolution for reliably calculating velocity gradients, the vertical profiles of  $\dot{\gamma}\Sigma\phi$  are of a rather poor quality near the bed surface (Figs. 6(b) and 6(c)), with some of the cylinder data not even exhibiting a pronounced maximum of  $\dot{\gamma}\Sigma\phi$ . For R22EXPl, we determine  $h$  from the most pronounced maximum and calculate the ratio  $R_h \equiv h/h^{R22}$ , where  $h^{R22}$  is the reported flow depth value. It was measured as the depth over the mean of the elevation at which the linear extrapolation of  $v_x(z)$  vanishes and the interpolated elevation at which the particle volume fraction  $\phi = 0.6$  [28]. Since this method requires neither particle velocity data inside the sediment bed nor calculating particle velocity gradients,  $h^{R22}$  is more much precisely determinable than  $h$ . The value of  $R_h$  varies, indeed, little with flow conditions for R22EXPl, between about  $\min(R_h) = 0.91$  and  $\max(R_h) = 1.02$ . Assuming that, under hypothetically experimentally ideal conditions,  $R_h$  does not depend on the flow condition, we use it to obtain  $\tau_b$  and its uncertainty range from the estimate  $\tilde{\tau}_b^{R22} = \tilde{\tau}_b(h^{R22})$  for both R22EXPl and R22EXPc as follows:

$$\begin{aligned} \tau_b &= \frac{1}{2} [\max(R_h) + \min(R_h)] \tilde{\tau}_b^{R22} \\ &\pm \frac{1}{2} [\max(R_h) - \min(R_h)] \tilde{\tau}_b^{R22}. \end{aligned} \quad (37)$$

### Z22LESw

The values of  $h^*$  reported for this data set are based on Eq. (35) [12]. We therefore use the reported values of  $h^*$  and  $\Theta$ , assuming that the uncertainty of  $\Theta$  is very small (smaller than the respective symbols in the plots).

For these data sets, we use the reported values of  $h$  as its effect on  $\tau_b$  is very small because of very small width-to-depth ratios ( $b/h \approx 0.1$ ) and because  $h$  was much larger than the bedload thickness [12–14]. For the numerical data sets Z22LESn and Z23LES, we therefore conclude that the uncertainty of  $\tau_b$  is very small (smaller than the respective symbols in the plots). For the experimental data sets D23EXPx, the main source of uncertainty comes from the determination of the slope angle  $\alpha$ . We propagate its reported uncertainty to estimate the uncertainty of  $\tau_b$ .

### Z21DNS and KU17DNS

As we do not have access to the raw data of these data sets, and since  $h$  was much larger than the bedload thickness [25, 26], we use the reported values of  $h^*$  and  $\Theta$ , assuming that the uncertainty of  $\Theta$  is very small (smaller than the respective symbols in the plots).

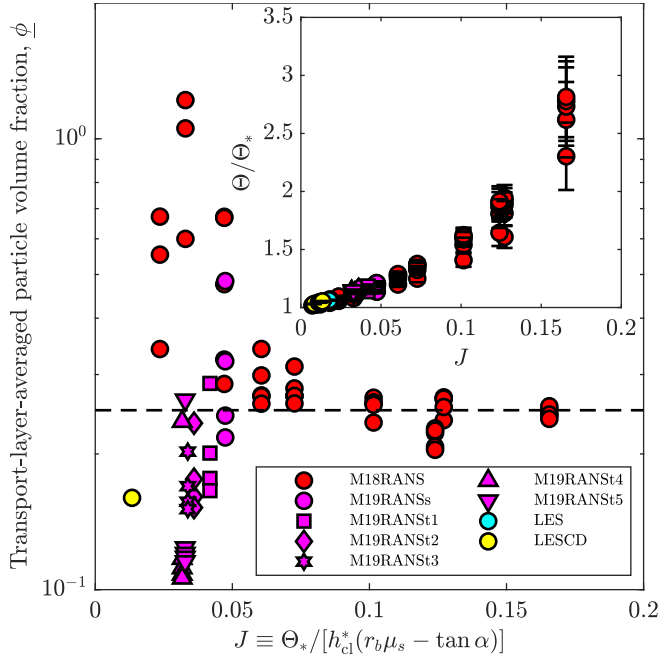


FIG. 8. Transport-layer-averaged particle volume fraction  $\phi$ , calculated from the  $Q_*$ -data as described in the text, versus  $J$ . Symbols correspond to grain-unresolved CFD-DEM simulations (Table I). The dashed line indicates the value  $\phi = 0.25$  exhibited for large  $J$ , where the ratio  $\Theta/\Theta_*$  deviates from unity the most. Inset: Estimate of  $\Theta/\Theta_*$  resulting from  $\phi = 0.25$ , where the error bars correspond to the propagated uncertainty of  $\mu_s$ , required for predicting  $M_*$  and therefore  $\Theta$ , as described in the text.

For these data sets, we determine  $h^*$  and subsequently  $\Theta$  from  $\Theta_*$  and  $h_{cl}^*$ , both of which can be determined with negligible uncertainty. In order to determine  $\Theta$  using Eq. (26), one needs to know the value of  $\phi$ . To this end, we calculate  $M_*$  from the  $Q_*$ -data via Eq. (1), using the predicted value of  $\Theta_t$  from Eq. (3), and subsequently  $\phi$  from  $M_*$ ,  $\Theta_*$ , and  $h_{cl}^*$  via Eq. (26). Figure 8 shows the resulting behavior of  $\phi$  as a function of  $J \equiv \Theta_*/[h_{cl}^*(r_b\mu_s - \tan \alpha)]$ . We are interested in the value of  $\phi$  in the limit of large  $J$ , since the ratio  $\Theta/\Theta_*$  deviates the more from unity the larger  $J$  (inset of Fig. 8). It can be seen that, in this limit,  $\phi \approx 0.25$ . This value is reasonable as it is about half of  $\phi(0)$  for intense transport conditions [18].

Although we use the  $M_*$ -values calculated from the  $Q_*$ -data for the determination of  $\phi$ , we do not do so when estimating  $\Theta$ , in order to avoid an implicit dependence of  $\Theta$  on  $Q_*$ . Instead, we obtain  $\Theta$  from the values of  $M_*$  predicted by Eq. (33b) with  $\phi = 0.25$ . The uncertainty of  $\Theta$  in Figs. 4(b) and 4(c), and subsequently that of  $\Theta^{D23}$  in Figs. 4(a), then corresponds to the propagated uncertainty of  $\mu_s$  in the calculation of  $\Theta$  via Eqs. (26) and (33b).

### BLRANSx

For these data sets,  $h^* = \infty$  by construction and  $\Theta$  is a preset parameter (no uncertainty).

### DRAG COEFFICIENT

#### Sphere-normalized drag coefficient after Deal et al. [14]

Deal et al. [14] defined the sphere-normalized drag coefficient  $C^*$  as

$$C^* \equiv S_f v_o^2 / v_s^2, \quad (38)$$

where  $v_s$  is the grain settling velocity and  $v_o$  its theoretical values for spheres, given by [14, 56]

$$v_{o*} = -3.81564 + 1.94593D_* - 0.09016D_*^2 - 0.00855D_*^3 + 0.00075D_*^4, \quad (39)$$

with  $v_{o*} \equiv \log_{10} v_o^3 / [(s-1)g\nu]$ ,  $D_* \equiv \log_{10}(s-1)gd_o^3/\nu^2$ , and  $d_o$  the sphere-equivalent grain diameter (note that  $d_o \neq d$ ).

### Drag coefficient in experiments and grain-resolved CFD-DEM simulations

The drag coefficient  $C_D$  in Eq. (3) parametrizes the effective streamwise drag force acting on grains. It is smaller than that for settling grains,  $C_{D\text{Settle}} = 4(s-1)gd/(3v_s^2)$  [14], due to the smaller projected area exposed to the flow. Assuming again that transported grains tend to align their largest projected area  $A_p^{\text{max}} = \pi ab/4$  parallel to the bed, the effective projected area  $A_p^{\text{eff}}$  in the streamwise direction is estimated as the geometric mean of the remaining two projected areas  $\pi ac/4$  and  $\pi bc/4$ :  $A_p^{\text{eff}} = \pi\sqrt{abc}/4$ , implying  $A_p^{\text{eff}}/A_p^{\text{max}} = c/\sqrt{ab} \equiv S_f$ , which is the Corey shape factor. Hence, in spite of a different physical reasoning, we arrive at the same expression as Ref. [14]:  $C_D = S_f C_{D\text{Settle}}$  or

$$C_D = 4S_f(s-1)gd/(3v_s^2). \quad (40)$$

However, note that the values of  $C_D$  for non-spherical grains differ from those in Ref. [14] due to a different definition of  $d$ .

### Drag coefficient in grain-unresolved CFD-DEM simulations

The numerical CFD-DEM models that do not resolve the sub-grain scale rely on semiempirical relations for fluid-particle interactions. They consider buoyancy and drag forces on spheres or composite grains consisting of non-overlapping component spheres, but neglect lift forces. Following Ref. [57], the drag force is modeled as the total force on all component spheres:

$$\mathbf{F}_D = \sum_i \frac{1}{8} \rho_f \pi d_i^2 \left[ \left( \frac{\Re_c \nu}{d_i \epsilon^{p_1}} \right)^{1/m} + \left( \frac{C_D^\infty |\mathbf{u}_r|}{\epsilon^{p_2}} \right)^{1/m} \right]^m \mathbf{u}_r, \quad (41)$$

where  $d_i$  is the diameter of the  $i$ -th component sphere,  $\mathbf{u}_r$  the fluid-particle velocity difference, and  $\Re_c$ ,  $C_D^\infty$ ,  $m$ ,  $p_1$ , and  $p_2$  are empirical parameters (Table II). Dividing

Numerical model	$\Re_c$	$C_D^\infty$	$m$	$p_1$	$p_2$
Maurin et al. [37]	24.4	0.4	1	3.1	3.1
Durán et al. [36] (nominal)	24	0.5	2	0	0
Durán et al. [36] (enhanced drag)	96	2	2	0	0
Xie et al. [38] (nominal)	23.04	0.3969	2	$p$	$p-1$
Xie et al. [38] (enhanced drag)	69.12	1.1907	2	$p$	$p-1$

TABLE II. Summary of drag law parameters used in grain-unresolved CFD-DEM simulations of bedload transport, where  $p = 3.7 - 0.65 \exp[-(1.5 - \log_{10}(\epsilon |\mathbf{u}_r| d_i / \nu))^2 / 2]$ .

Eq. (41) by the grain weight  $\frac{\pi}{6} \sum_i d_i^3$  leads to an expression for the ratio between the drag acceleration  $\mathbf{a}_D$  and submerged gravity  $\tilde{g} \equiv (1 - 1/s)g$  in terms of nondimen-

sionalized quantities:

$$\frac{\mathbf{a}_D}{\tilde{g}} = \frac{3}{4} \left[ \left( \frac{\Re_c}{\widetilde{G} a \epsilon^{p_1}} \right)^{1/m} + \left( \frac{C_D^\infty |\tilde{\mathbf{u}}_r|}{\epsilon^{p_2}} \right)^{1/m} \right]^m \tilde{\mathbf{u}}_r, \quad (42)$$

where  $\tilde{\mathbf{u}}_r \equiv \mathbf{u}_r / \sqrt{s \tilde{g} d}$ , with  $d \equiv \frac{3}{2} V_p / A_p^{\text{max}} = \sum_i d_i^3 / \sum_i d_i^2$ , is the nondimensionalized fluid-particle velocity difference and

$$\widetilde{G} a \equiv \frac{\sqrt{(\sum_i d_i^2)(\sum_i d_i^3)}}{\sum_i d_i} \sqrt{s \tilde{g} / \nu} \quad (43)$$

a quantity similar to the Galileo number. From Eq. (42), one obtains the nondimensionalized settling velocity  $\tilde{v}_s$  of a single composite grain in quiescent fluid ( $\epsilon = 1$ ) as [41]

$$\tilde{v}_s = \left[ \sqrt{\frac{1}{4} \sqrt{\left( \frac{\Re_c}{C_D^\infty \widetilde{G} a} \right)^2 + \frac{4}{3 C_D^\infty}} - \frac{1}{2} \sqrt{\frac{\Re_c}{C_D^\infty \widetilde{G} a}}} \right]^m \quad (44)$$

and subsequently the drag coefficient as

$$C_D = \frac{4(s-1)gd}{3v_s^2} = \frac{4}{3\tilde{v}_s^2}. \quad (45)$$

Here we used that a composite grain is treated as if the projected area of all its component spheres is always, regardless of its orientation relative to the flow, fully exposed to the flow, which follows from Eq. (41). That is, the total projected area seen by the flow,  $A_p = \frac{\pi}{4} \sum_i d_i^2$ , is constant, and therefore  $A_p^{\text{eff}} = A_p^{\text{max}}$ .

### Correction of mistake made by Zhang et al. [13]

In a part of their data (Z23LES in Table I), these authors artificially shrank the grain size seen by the fluid solver (but not the actual size) and observed an increasing settling velocity  $v_s$  as a result. They argued that this increase originates from a lower drag force and thus  $C_D$ . However, they forgot to account for the fact that their shrinkage procedure also lowers the particle volume and therefore the buoyancy force. Figure 9 shows that the latter can nearly entirely quantitatively explain their observed increase of  $v_s$ , while  $C_D$  remains virtually unaffected. For this reason, we only show their data for unshrunk grains.

### DETERMINATIONS OF ANGLE OF REPOSE AND ITS UNCERTAINTY

We acquired the same spheres as those used in Ref. [15] (NC18EXP in Table I) from the same company (Chiao Dar Acry & Advertisement Co., Ltd., <http://www.bridgeacry.com.tw>) and measured  $\mu_s$  using the funnel

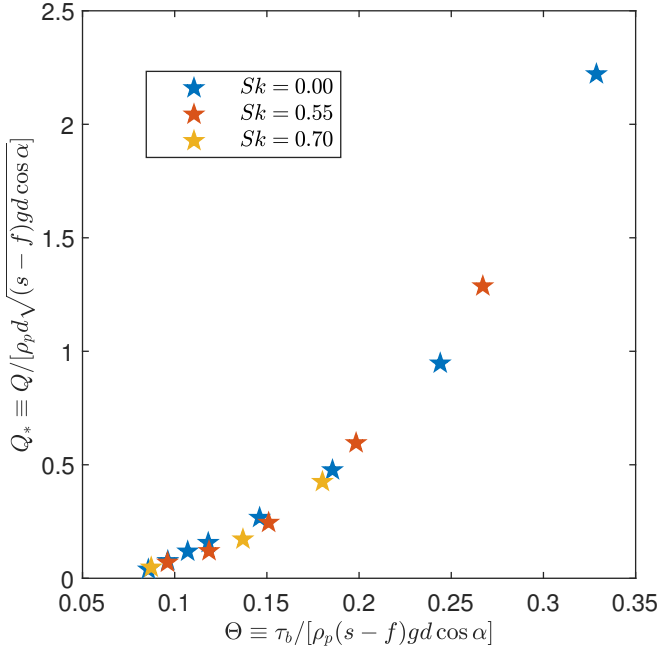


FIG. 9. LES-DEM simulation data [13] (Z23LES in Table I) for three different values of the grain shrinkage  $Sk$ , defined as in Ref. [13]. A value  $Sk > 0$  indicates that the fluid solver sees a shrunk grain, while the actual grain size remains the same. This artificial procedure affects the buoyancy force  $\rho_f V_p g$  calculated by the fluid solver via a reduction of the grain volume from  $V_p$  to  $fV_p$ , with  $f < 1$  the volume ratio, implying that  $\Theta$  and  $Q_*$  must be redefined as  $\Theta \equiv \tau_b / [\rho_p (s - f) g d \cos \alpha]$  and  $Q_* \equiv Q / [\rho_p d \sqrt{(s - f) g d \cos \alpha}]$ . Assuming shrinkage has no effect on the drag force, one obtains  $s - f = (s - 1)v_s^2 / v_{s0}^2$ , the expression used to calculate  $s - f$  in this figure, where  $v_s$  and  $v_{s0}$  are the settling velocities of the shrunk and original grain, respectively, both reported in Ref. [13]. The fact that this expression collapses the data for different  $Sk$  implies that, indeed, the value of  $C_D$  is almost unaffected by shrinkage, in contrast to statements in Ref. [13].

method [34] in the manner described in Ref. [14] (Fig. 10). Furthermore, we confirmed with DEM simulations that different measurement methods have only a small effect on  $\mu_s$  provided that a sufficiently large number of grains is used and that there is some means of preventing grains from rolling away (such as a rim or a rough bed, see Fig. 11). Based on these simulations, we assign an uncertainty of 5% to all  $\mu_s$ -measurements, including those from different studies and methods.

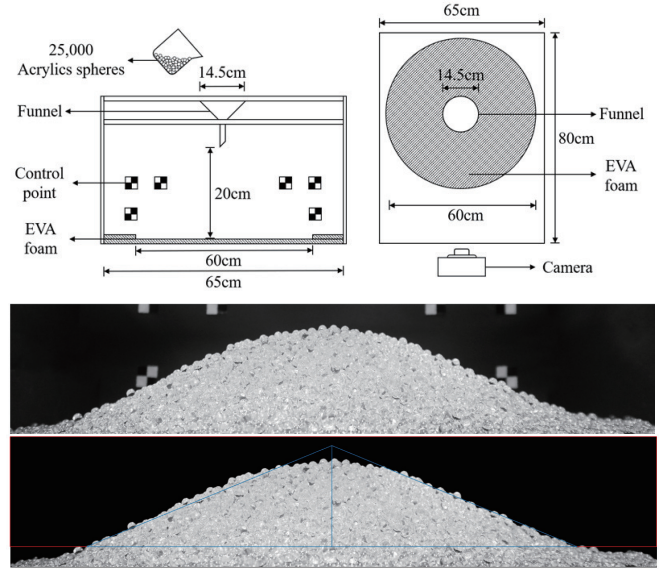


FIG. 10. Measurements of  $\mu_s$  for the data set NC18EXP [15] using the funnel method as described in Ref. [14]. We slowly poured 25,000 grains onto an elevated disk bounded by a  $2d$ -high rim. The angle of repose of the resulting heap is then determined as the base angle of the isosceles triangle that has the same area as the projected heap, averaged over two side-view images separated by a rotation of  $90^\circ$  [58].

Numerical model	$e_n$	$\mu_c$	$\mu_s$
Maurin et al. [37] (data from Ref. [29])	0.5	0.4	0.40
Maurin et al. [37] (data from Ref. [30])	0.5	0.5	0.49–0.72
Durán et al. [36]	0.9	0.5	0.38
Xie et al. [38]	0.3	0.5	0.49

TABLE III. Normal restitution coefficient  $e_n$  and tangential contact friction coefficient  $\mu_c$  used in grain-unresolved CFD-DEM simulations of bedload transport. The tangent of the static angle of repose,  $\mu_s$ , has been determined as described in Fig. 11.

### CONTACT PARAMETERS AND $\mu_s$ IN GRAIN-UNRESOLVED CFD-DEM SIMULATIONS

\* 0012136@zju.edu.cn  
 † pengphu@zju.edu.cn  
 ‡ hezhiguo@zju.edu.cn

[1] V. Poggiali, M. Mastrogiuseppe, A. G. Hayes, R. Seu, S. P. D. Birch, R. Lorenz, C. Grima, and J. D. Hofgartner, Liquid-filled canyons on titan, *Geophysical Research Letters* **43**, 7887 (2016).  
 [2] F. Charru, B. Andreotti, and P. Claudin, Sand ripples and dunes, *Annual Review of Fluid Mechanics* **45**, 469 (2013).  
 [3] O. Durán Vinent, B. Andreotti, P. Claudin, and C. Winter, A unified model of ripples and dunes in water

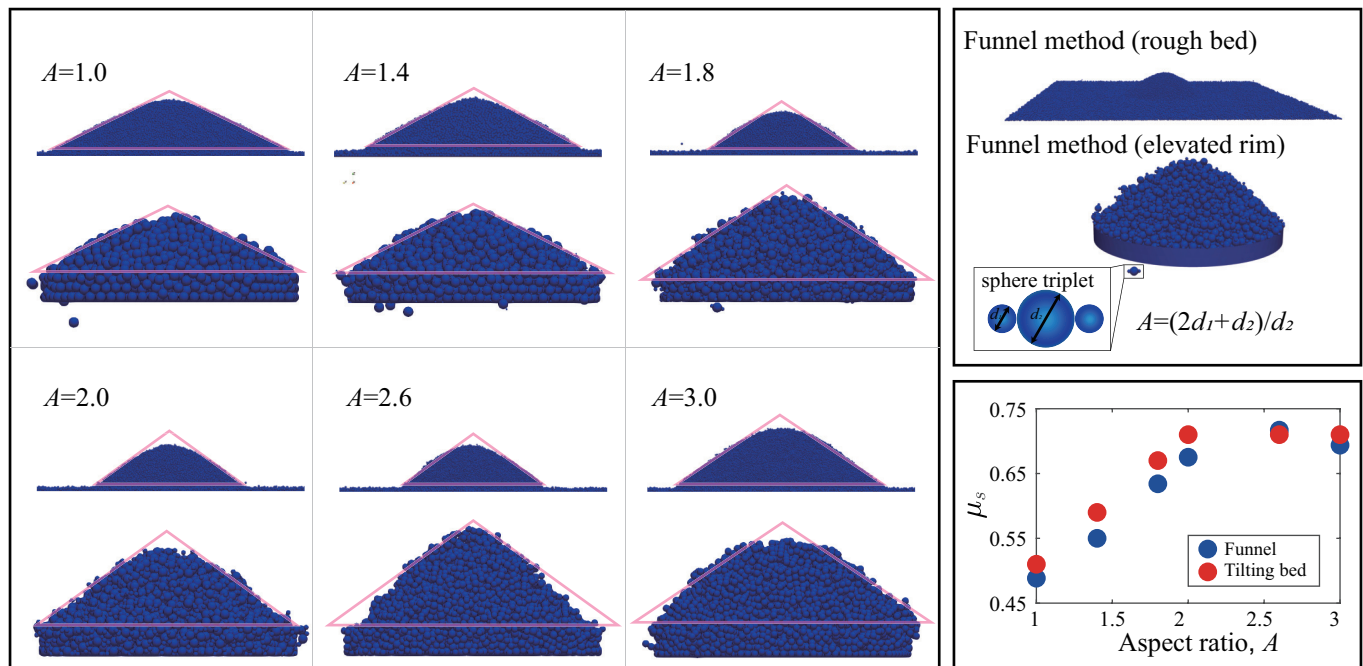


FIG. 11. We compare three different methods of measuring the tangent of the static angle of repose,  $\mu_s$ , for the composite grains (spheres and sphere triplets) used in the grain-unresolved DEM-CFD simulations: slowly pouring a sufficient number of grains onto a rough bed consisting of spheres of the same sphere-equivalent diameter  $d_0$  (funnel method 1), onto an elevated disk of diameter  $24d_0$  bounded by a  $2d_0$ -high rim (funnel method 2, exactly as described in Ref. [14]), and tilting the granular bed until the granular bulk moves (tilting method). The most reliable and reproducible results are yielded by funnel method 1, where the angle of repose is determined as the base angle of the isosceles triangle that has the same area as the projected heap, averaged over two side-view images separated by a rotation of  $90^\circ$  [58]. For funnel method 2, the heaps exhibit too irregular shapes when the aspect ratio  $A$  becomes too large, making a clear determination of the angle of repose difficult. However, for  $A \lesssim 2$ , it yields values very close to funnel method 1. The tilting method also yields similar results as funnel method 1, though it is sometimes difficult to distinguish between bulk and isolated-grain motion. We therefore decided to use funnel method 1 as the standard procedure to determine  $\mu_s$  in the grain-unresolved DEM-CFD simulations.

- and planetary environments, *Nature Geoscience* **12**, 345 (2019).
- [4] V. R. Baker, C. W. Hamilton, D. M. Burr, V. C. Gulick, G. Komatsu, W. Luo, J. W. Rice, and J. Rodriguez, Fluvial geomorphology on Earth-like planetary surfaces: A review, *Geomorphology* **245**, 149 (2015).
- [5] J. Schieber, Mud re-distribution in epicontinental basins – Exploring likely processes, *Marine and Petroleum Geology* **71**, 119 (2016).
- [6] A. Shchepetkina, M. K. Gingras, M. G. Mángano, and L. A. Buatois, Fluvio-tidal transition zone: Terminology, sedimentological and ichnological characteristics, and significance, *Earth-Science Reviews* **192**, 214 (2019).
- [7] P. Frey and M. Church, How river beds move, *Science* **325**, 1509 (2009).
- [8] A. Recking, A comparison between flume and field bed load transport data and consequences for surface-based bed load transport prediction, *Water Resources Research* **46**, W03518 (2010).
- [9] B. Dhont and C. Ancey, Are bedload transport pulses in gravel bed rivers created by bar migration or sediment waves?, *Geophysical Research Letters* **45**, 5501 (2018).
- [10] E. M. Yager, J. G. Venditti, H. J. Smith, and M. W. Schmeckle, The trouble with shear stress, *Geomorphology* **323**, 41 (2018).
- [11] J. Guo, Sidewall and non-uniformity corrections for flume experiments, *Journal of Hydraulic Research* **53**, 218 (2015).
- [12] Q. Zhang, E. Deal, J. T. Perron, J. G. Venditti, S. J. Benavides, M. Rushlow, and K. Kamrin, Fluid-driven transport of round sediment particles: From discrete simulations to continuum modeling, *Journal of Geophysical Research: Earth Surface* **127**, e2021JF006504 (2022).
- [13] Q. Zhang, E. Deal, J. T. Perron, J. G. Venditti, S. J. Benavides, M. Rushlow, and K. Kamrin, Discrete simulations of fluid-driven transport of naturally shaped sediment particles, *ESS Open Archive* 10.22541/essoar.168500367.77673037/v1 (2023).
- [14] E. Deal, J. G. Venditti, S. J. Benavides, R. Bradley, Q. Zhang, K. Kamrin, and J. T. Perron, Grain shape effects in bed load sediment transport, *Nature* **613**, 298 (2023).
- [15] W. J. Ni and H. Capart, Stresses and drag in turbulent bed load from refractive index-matched experiments, *Geophysical Research Letters* **45**, 7000 (2018).
- [16] G. Gioia and F. A. Bombardelli, Scaling and similarity in rough channel flows, *Physical Review Letters* **88**, 014501 (2002).
- [17] G. Gioia and Pinaki Chakraborty, Turbulent friction in rough pipes and the energy spectrum of the phenomono-



- logical theory, *Physical Review Letters* **96**, 044502 (2006).
- [18] T. Pähtz and O. Durán, Universal friction law at granular solid-gas transition explains scaling of sediment transport load with excess fluid shear stress, *Physical Review Fluids* **3**, 104302 (2018).
- [19] T. Pähtz and O. Durán, Unification of aeolian and fluvial sediment transport rate from granular physics, *Physical Review Letters* **124**, 168001 (2020).
- [20] C. Ancey, Bedload transport: a walk between randomness and determinism. Part 1. The state of the art, *Journal of Hydraulic Research* **58**, 1 (2020).
- [21] P. Frey, M. Dufresne, T. Böhm, M. Jodeau, and C. Ancey, Experimental study of bed load on steep slopes, in *River Flow 2006* (Taylor & Francis Group, London, UK, 2006) pp. 887–893.
- [22] P. Frey, Particle velocity and concentration profiles in bedload experiments on a steep slope, *Earth Surface Processes and Landforms* **39**, 646 (2014).
- [23] A. Armanini and V. Cavedon, Bed-load through emergent vegetation, *Advances in Water Resources* **129**, 250 (2019).
- [24] V. Carrillo, J. Petrie, L. Timbe, E. Pacheco, W. Astudillo, C. Padilla, and F. Cisneros, Validation of an experimental procedure to determine bedload transport rates in steep channels with coarse sediment, *Water* **13**, 672 (2022).
- [25] R. Jain, S. Tschisgale, and J. Fröhlich, Impact of shape: Dns of sediment transport with non-spherical particles, *Journal of Fluid Mechanics* **916**, A38 (2021).
- [26] A. G. Kidanemariam and M. Uhlmann, Formation of sediment patterns in channel flow: minimal unstable systems and their temporal evolution, *Journal of Fluid Mechanics* **818**, 716 (2017).
- [27] R. Zhu, Z. He, K. Zhao, B. Vowinkel, and E. Meiburg, Grain-resolving simulations of submerged cohesive granular collapse, *Journal of Fluid Mechanics* **942**, A49 (2022).
- [28] D. Rebai, D. Berzi, F. Ballio, and V. Matousek, Experimental comparison of inclined flows with and without intense sediment transport: Flow resistance and surface elevation, *Journal of Hydraulic Engineering* **148**, 04022026 (2022).
- [29] R. Maurin, J. Chauchat, and P. Frey, Revisiting slope influence in turbulent bedload transport: consequences for vertical flow structure and transport rate scaling, *Journal of Fluid Mechanics* **839**, 135 (2018).
- [30] R. Monthiller, *Particle shape influence on turbulent bedload transport*, Master’s thesis, ENSEEIHT, University of Toulouse, Toulouse, France (2019).
- [31] H. A. Einstein, Formulas for the transportation of bedload, *Transactions of ASCE* **107**, 561 (1942).
- [32] J. W. Johnson, The importance of considering sidewall friction in bed-load investigations, *Civil Engineering* **12**, 329 (1942).
- [33] J. Guo, Exact procedure for Einstein-Johnson’s sidewall correction in open channel flow, *Journal of Hydraulic Engineering* **143**, 06016027 (2017).
- [34] H. M. Beakawi Al-Hashemi and O. S. Baghabra Al-Amoudi, A review on the angle of repose of granular materials, *Powder Technology* **330**, 397 (2018).
- [35] V. Matoušek and Š. Zrostlík, Collisional transport model for intense bed load, *Journal of Hydrology and Hydromechanics* **68**, 60 (2020).
- [36] O. Durán, B. Andreotti, and P. Claudin, Numerical simulation of turbulent sediment transport, from bed load to saltation, *Physics of Fluids* **24**, 103306 (2012).
- [37] R. Maurin, J. Chauchat, B. Chareyre, and P. Frey, A minimal coupled fluid-discrete element model for bedload transport, *Physics of Fluids* **27**, 113302 (2015).
- [38] J. Xie, P. Hu, T. Pähtz, Z. He, and N. Cheng, Fluid-particle interaction regimes during the evolution of turbidity currents from a coupled les/dem model, *Advances in Water Resources* **163**, 104171 (2022).
- [39] R. Jain, S. Tschisgale, and J. Fröhlich, Effect of particle shape on bedload sediment transport in case of small particle loading, *Meccanica* **55**, 299 (2020).
- [40] A. H. Clark, M. D. Shattuck, N. T. Ouellette, and C. S. O’Hern, Role of grain dynamics in determining the onset of sediment transport, *Physical Review Fluids* **2**, 034305 (2017).
- [41] T. Pähtz, Y. Liu, Y. Xia, P. Hu, Z. He, and K. Tholen, Unified model of sediment transport threshold and rate across weak and intense subaqueous bedload, windblown sand, and windblown snow, *Journal of Geophysical Research: Earth Surface* **126**, e2020JF005859 (2021).
- [42] W. S. Chepil, The use of spheres to measure lift and drag on wind-eroded soil grains, *Soil Science Society of America Journal* **25**, 343 (1961).
- [43] W. S. Chepil, The use of evenly spaced hemispheres to evaluate aerodynamic forces on a soil surface, *Transcripts of the American Geophysical Union* **39**, 397 (1958).
- [44] T. Pähtz and K. Tholen, General average balance equations for a mixture of rigid particles and a continuous fluid, arXiv:2308.09661v2 (2024).
- [45] A. G. Kidanemariam, *The formation of patterns in subaqueous sediment*, Ph.D. thesis, Karlsruhe Institute of Technology, Karlsruhe, Germany (2016).
- [46] R. Antonia and B. Pearson, Reynolds number dependence of velocity structure functions in a turbulent pipe flow, *Flow, Turbulence and Combustion* **64**, 95 (2000).
- [47] H. Tennekes and J. L. Lumley, *A First Course in Turbulence* (MIT Press, Cambridge, MA, 1972).
- [48] T. Song, *Velocity and turbulence distribution in nonuniform and unsteady open-channel flow*, Ph.D. thesis, Swiss Federal Institute of Technology EPFL, Lausanne, Switzerland (1994).
- [49] T. Song and Y. M. Chiew, Turbulence measurement in non-uniform open-channel flow using acoustic Doppler velocimeter (ADV), *Journal of Engineering Mechanics* **127**, 219 (2001).
- [50] C. Auel, I. Albayrak, and R. M. Boes, Turbulence characteristics in supercritical open channel flows: Effects of froude number and aspect ratio, *Journal of Hydraulic Engineering* **140**, 04014004 (2014).
- [51] S. Q. Yang, S. Y. Lim, and J. A. McCorquodale, Investigation of near wall velocity in 3-d smooth channel flows, *Journal of Hydraulic Research* **43**, 149 (2005).
- [52] T. Loiseleux, P. Gondret, M. Rabaud, and D. Doppler, Onset of erosion and avalanche for an inclined granular bed sheared by a continuous laminar flow, *Physics of Fluids* **17**, 103304 (2005).
- [53] R. A. Bagnold, The flow of cohesionless grains in fluid, *Philosophical Transactions of the Royal Society London A* **249**, 235 (1956).
- [54] J. Chauchat, A comprehensive two-phase flow model for unidirectional sheet-flows, *Journal of Hydraulic Research* **56**, 15 (2018).

- [55] F. Boyer, É. Guazzelli, and O. Pouliquen, Unifying suspension and granular rheology, *Physical Review Letters* **107**, 188301 (2011).
- [56] W. E. Dietrich, Settling velocity of natural particles, *Water Resources Research* **18**, 1615 (1982).
- [57] R. Sun, H. Xiao, and H. Sun, Realistic representation of grain shapes in CFD-DEM simulations of sediment transport with a bonded-sphere approach, *Advances in Water Resources* **107**, 421 (2017).
- [58] F. Elekesa and E. J. R. Parteli, An expression for the angle of repose of dry cohesive granular materials on earth and in planetary environments, *Proceedings of the Na-*

*tional Academy of Sciences of the United States of America* **118**, e2107965118 (2021).

#### ACKNOWLEDGEMENTS

T.P. acknowledges support from the National Natural Science Foundation of China (nos. 12350710176 and 12272344). O.D. acknowledges support from the Texas A&M Engineering Experiment Station. Z.H. acknowledges support from the National Natural Science Foundation of China (no. 52171276).